Comparing mountain breezes and their impacts on CO2 mixing ratios at three contrasting areas

C. Román-Cascón, C. Yagüe, J.A. Arrillaga, M. Lothon, E.R. Pardyjak, Fabienne Lohou, R.M. Inclán, M. Sastre, G. Maqueda, S. Derrien, et al.

Version of Record: https://www.sciencedirect.com/science/article/pii/S0169809519300596
Manuscript_43b11e643fafcb2e0b1f0f3de2ccf16a

Comparing mountain breezes and their impacts on CO_2 mixing ratios at three sites

C. Román-Cascón[a,b], C. Yagüe[a], J.A. Arrillaga[a], M. Lothon[b], E. R. Pardyjak[c], F. Lohou[b], R. M. Inclán[d], M. Sastre[a], G. Maqueda[a], S. Derrien[b], Y. Meyerfeld[b], C. Hang[c,e], P. Campargue-Rodríguez[b], I. Turki[b]

[a]*Departamento de Física de la Tierra y Astrofísica. Universidad Complutense de Madrid, Spain.*
[b]*Laboratoire d'Aérologie, Université Toulouse Paul Sabatier, CNRS, France.*
[c]*Department of Mechanical Engineering, University of Utah, Salt Lake City, US.*
[d]*Department of Environment, CIEMAT, Madrid, Spain.*
[e]*Department of Civil Engineering, Monash University, Clayton, Victoria, Australia 3800.*

Abstract

This work presents the characterisation and comparison of daytime and nighttime mountain breezes observed at three sites through the analysis of tower data. The sites are located: (i) in the foothills of the Guadarrama Mountains in Spain, (ii) on a plateau adjacent to the Pyrenees in France, and (iii) in the Salt Lake Valley (SLV) in the southwest of the United States. The thermally-driven winds are detected through a systematic algorithm which considers both synoptic and local meteorological conditions. The characteristics of the mountain breezes depend on the scale of the breeze at each site. Nighttime events are associated with stronger wind speeds at the two sites located farther away from the mountains due to larger-scale phenomena (valley winds and mountain-plain winds). The arrival of both nighttime and daytime flows to the sites are observed approximately when the buoyancy heat flux changes sign, being a few hours delayed at the sites farther from the mountains.

In addition, the impacts of these breezes on CO_2 mixing ratios are analysed. The characteristic increase of CO_2 mixing ratio observed during the evening transition takes place approximately when the nocturnal breeze arrives at the site. Nonetheless, both processes are not always simultaneous, indicating that CO_2 advection is not the main mechanism controlling the drastic CO_2 increase. An analogous result is obtained for the CO_2 decrease at the morning transition. However, we have found that the CO_2 mixing ratio is sensitive to wind direction (horizontal advection) in highly heterogeneous areas like the SLV, where CO_2 emissions from the nearby city centre play an important role.

Finally, a clear relationship is found between the CO_2 mixing ratio and near-surface turbulence at night. Maximum CO_2 mixing ratios are found for specific turbulence thresholds, which depend on the height of the CO_2 sensor. Conditions associated with both stronger and weaker turbulence levels lead to reduced CO_2 mixing ratios at the local measurement height due to excessive and ineffective mixing, respectively.

Keywords:
Thermally-driven flows, downslope, upslope, CO_2, advection, turbulent mixing

---

Email address: carlosromancascon@ucm.es (C. Román-Cascón)

1. Introduction

Thermally-driven mountain winds appear under weak-synoptic forcing in mountainous regions and even in areas with gentle slopes (Mahrt, 2017). These winds are driven by the pressure gradient generated by horizontal temperature differences in the presence of different topographical configurations like slopes, valleys, or mountains (Whiteman, 2000). They have different scales depending on the extent of the region affected by the temperature differences and on the local topographical features. For example, slope flows form due to differences in temperature between two locations over a slope at the same altitude but at different heights from the surface. Valley-winds are partially the result of the channelling of slope flows at the bottom of valleys. Mountain-plain winds are more associated with the mesoscale dimensions of mountain ridges (Martínez et al., 2010; Zardi and Whiteman, 2013). These different-scale mountain breezes can be observed alone or as interactions amongst these various types. Some of these winds have been relatively well studied in areas such as the Alps (Rotach et al., 2004; Nadeau et al., 2013) and the Salt Lake Valley (Doran et al., 2002; Monti et al., 2002; Whiteman and Zhong, 2008). However, despite their common character under fair-weather conditions, long-term statistical characterisations are rare. Most of the studies focus on the analysis of relatively short periods of time and at specific locations, with a subjective choice of the analysed events. Only a few long-term analyses exist over well-studied regions (e.g. Stewart et al., 2002, in the western US). In addition, an appropriate and systematic comparison between mountain-breezes characteristics at different sites is missing. This lack of systematic climatologies at diverse sites and their comparison is the primary motivation for this study.

The arrival of these winds are normally characterized by sudden changes in wind direction, blowing from the highest to the lowest elevations during the night and vice versa during the day. These flows (with variable thickness and location of the jet) change the local vertical and horizontal profiles of wind, temperature, or trace gases like water vapour or CO_2. This affects the representativeness of a point measurement (Román-Cascón et al., 2015; Stiperski and Rotach, 2016). With their arrival, the advected air can transport pollutants and humidity from distant sources and influence, for example, the formation of fog (Hang et al., 2016; Prtenjak et al., 2018). However, many questions remain open concerning the interactions of these flows with local stability conditions and turbulence close to the surface (Mahrt and Mills, 2009; Sun et al., 2015; Rotach et al., 2017; Serafin et al., 2018; Lehner and Rotach, 2018). This also makes accurate estimates of the CO_2 exchange between the land (soil and vegetation) and the air aloft more difficult. These exchanges are still considered the most uncertain term in the net global carbon budget (Rotach et al., 2014), even though land ecosystems are, together with the oceans, the most important sinks of CO_2 (Raupach, 2011; Yakir, 2017). Reducing this uncertainty is very important for the study of climate change, which is still one of the main problems facing society (Urry, 2015). Due to its importance, the United Nations Framework Convention on Climate Change recommended improved quantification of these sinks (Kyoto Protocol, 1997). In this context, a substantial effort has been undertaken in recent years to observe and monitor the carbon budget over land (and ocean), via efforts such as the FLUXNET network (Baldocchi et al.,

2001) or under the Integrated Carbon Observation System (ICOS) infrastructure (Gielen et al., 2017). Thus, many towers around the world are continuously measuring CO_2 mixing ratios and fluxes over different surfaces and climate types (Gilmanov et al., 2010). However, the interpretation of these CO_2 measurements needs to be based on the understanding of the different near-surface dynamical processes.

Several studies have focused on the interactions of mesoscale flows with CO_2 concentration and fluxes over heterogeneous and complex terrain, where the observational analysis and data interpretation is even more complicated. Sun et al. (1998) studied some of these influences in a region affected by a lake, analysing the impacts of lake breezes on CO_2, water vapour, and ozone transport. Eugster and Siegrist (2000) studied nocturnal CO_2 advection over non-flat, undulating terrain affected by katabatic cold-air drainage flows in Switzerland to understand and optimise the information provided by eddy covariance CO_2 fluxes (see also Baldocchi (2003)). Later, Sun et al. (2007) also showed how CO_2 advected by downslope and upslope flows dominated the net CO_2 transport through the analysis of three days in the Colorado Rocky Mountains. The importance of advection in the calculation CO_2 fluxes was even noted for small slopes by Kutsch et al. (2008) and by Araújo et al. (2008), who showed how horizontal variability of CO_2 stores (cold pools affected by drainage flows) should be considered during the night and during the morning transition in the Brazilian tropical forest. Other studies have focused on the effects of low-level jets on CO_2 fluxes and distribution (e.g. Karipot et al., 2006, 2008; Prabha et al., 2007) or, more specifically, on advection effect within a canopy (e.g. Staebler and Fitzjarrald, 2004; Alekseychik et al., 2013). All these works have dealt with the difficulties of interpreting limited observations at specific sites, an important issue that is partially improved by the use of numerical models. This has lead to numerous (and very different) CO_2 modelling studies in the last decades (e.g. Sun et al., 2006; Pino et al., 2012), some of them over complex-terrain (e.g. Sun et al., 2006; Uebel et al., 2017; Uebel and Bott, 2018).

Given these issues, future aims and the lack of climatological studies, this paper has two main interrelated objectives. The first objective is to characterise and compare diurnal mountain winds in three contrasting areas. This is achieved through an in-depth analysis of numerous daytime and nighttime events detected during relatively long periods, thanks to the availability of three high-quality datasets. The mountain breezes are detected using a systematic algorithm based on criteria similar to those in the algorithm presented in Arrillaga et al. (2018). The following three areas were analysed: (i) a site in foothills of the Guadarrama Mountains (Madrid, Spain), (ii) a site on a plateau close to the Pyrenees mountains (Lannemezan, France), and (iii) a site within the Salt Lake Valley (Utah, US) during the MATERHORN field campaign (Fernando et al., 2015). These sites have interesting differences in terms of topographical complexity, distance to the nearby mountains, and land use heterogeneities. However, similar recurrent nighttime/daytime flows patterns appear at each site, which motivates the systematic and identical data analysis presented here. The second objective takes advantage of this in-depth statistical characterisation of mountain breezes and aims to investigate the effect of these phenomena on the observed CO_2 mixing ratio.

The paper is organised as follows: Section 2 presents the sites and the data; Section

3 explains the algorithm used for the mountain breezes detection. Section 4 presents the characteristics of the mountain breezes at the three sites while Section 5 compares their main features. Their effects on CO_2 are analysed in Section 6. Finally, Section 7 summarises the main results and conclusions.

2. Observational sites

In this section, the three experimental sites are described. Each site is influenced by mountains with significantly different characteristics.

a. *La Herrería* site (hereafter indicated as HER): 40.582° N; 4.137° W, 920 m above sea level (asl) (Figure 1a). This site is in the foothills of Mount Abantos (1753 m), a prominent peak in the Guadarrama Mountain Range in central Spain (Durán et al., 2017). The site is just west of *El Escorial* and southeast of *San Lorenzo de El Escorial*. These are the only two towns within a 5 km radius and have approximate populations of 18000 and 15000, respectively. A 10-m tower was installed in *La Herreria Forest* over a surface composed of sparse herbaceous and shrub cover but surrounded by forest, particularly in the sector southwest of the site. The ecoregion (Olson et al., 2001) of the HER site belongs to the Iberian sclerophyllous and semi-deciduous forests (Mediterranean Forests, Woodlands and Scrub). The local topography immediatley surrounding the site of the tower is relatively flat (slope angle of less than 2° with a radius of a few meters), the slope increases considerably at the base of Mount Abantos, ≈ 2 km northwest of the site (see Figure 1a). Other mountains are present to the north and southwest of the site, but their influence is negligible in terms of downslope flows at the specific HER site.

b. Pyrenees site (hereafter indicated as CRA): 43.124° N; 0.362° E, 600 m asl (Figure 2a). This site is located in southern France, over the relatively flat (10 x 10 km area) Lannemezan Plateau, which is approximately 40 km north of the highest peaks in the Pyrenees (Lothon et al., 2014). Measurements used in this study were taken from a permanent 60-m tower at the Atmospheric Research Centre (CRA). This observatory is close to Lannemezan, a city of ≈6000 inhabitants located mostly to the east of the site (see Figure 2a). An industrial area is located in a sector 4 km to south-southeast of the site and a highway south of the site, both possibly influencing the CO_2 measured during the nighttime breezes. The tower is immediately surrounded by a mosaic of shrub, grass, crops and forest (especially in the sector to the south). The ecoregion of this site is characterised as Pyrenees conifer and mixed forests and Western European broadleaf forests (European-Mediterranean montane forests) (Olson et al., 2001). Regarding the topography, the local and regional (Pyrenees scale) slopes increase towards the south-southeast, with the base of the first-line of mountains at around 11 km south of the tower location. An important topographical feature of the region is the Aure Valley, a 30-km long north-south oriented valley that descends from 850 to 580 m asl (marked as "Valley end" in Figure 2a, located 11 km from CRA site). The valley is surrounded by steep mountains with peaks of around 1500-2000 m. Downslope winds from these mountains are channelled through the valley during nighttime as a downvalley flow, as found in the modelling study of Jiménez and Cuxart (2014).

c. Salt Lake Valley site (hereafter indicated as SLV): 40.799° N; 112.067° W, 1389 m asl (Figure 3a). This site corresponds to one of the experimental sites of the MATERHORN-Fog field campaign (Gultepe et al., 2016), which took place at different sites in northern Utah (US) from 27 December 2014 to 30 July 2015. A 20-m tower was installed at the SLV site during the period of the field campaign. The tower was positioned over very flat and smooth terrain composed of shrub and grass (ecoregion Great Basin shrub steppe (Olson et al., 2001)). The Great Salt Lake was 6 km west of the tower, clearly influencing the measurements. In addition, the Salt Lake City metropolitan area (population of over 1 million) was located east-southeast of the tower (see Figure 3a). The (mostly) urbanized valley is almost completely surrounded by mountains. The Wasatch Range (located in the NE-S tower sector) has the highest peaks. The closest distance to these mountains from the tower is 13 km to the east, while the farthest point is 35 km to the southeast (see Figure 3a). The Oquirrh Mountains are located S-SW of the tower site (10 km to the base and 20 km to the ridge) and Frary Peak (2010 m asl) is on Antelope Island, 15 km northwest of the tower. All these mountain ranges and the Great Salt Lake make this site the most complex one in terms of topography and interaction between different thermally generated flows.

This work uses specific variables (Table 1) obtained from the instrumentation deployed on the towers at each site including: wind direction (wd), wind speed (ws), CO_2 mixing ratio, buoyancy heat flux (H), turbulent kinetic energy (TKE), and rainfall. The data have been uniformly averaged over 30-min periods in the three cases (daily data for the rainfall). However, since the management of each experimental site belongs to different research groups and institutions, some differences exist on the instrumentation (Table 1), but this is not a significant drawback for the analysis.

Additionally, we use data from NCEP FNL (Final) Operational Global Analysis at the closest pixel of each location. These data are used for the detection of days with appropriate synoptic conditions for the development of mountain breezes. The selected variables are horizontal wind components (u, v), relative humidity, and temperature at the height of 700 hPa, obtained with a horizontal resolution of 1° (0.25° when available) every 6 h.

3. Mountain-breezes detection algorithm

In order to detect mountain-breeze events systematically, we have adapted an existing detection algorithm used in previous studies (Arrillaga et al., 2016, 2018). The first part of the algorithm successively applies the following filters to data acquired from NCEP FNL (at 700 hPa) as well as local rainfall information to identify days with synoptic and local-weather conditions that are conducive to mountain breeze formation:

1. Filter 1: Only those days with synoptic wind speed (daily mean) at 700 hPa lower than 9 m s^{-1} (10 m s^{-1} at the SLV site) are retained (low synoptic-pressure gradient). These values have been changed from others used in Arrillaga et al. (2016, 2018). The height of 700 hPa has been used instead of 850 hPa to avoid the influence of the mountains. The 9 (10) m s^{-1} threshold has been selected after different sensitivity experiments at each site.

2. Filter 2: From days passing filter 1, only those with equivalent potential temperature variation at 700 hPa greater than -1.45 K in 6 h are retained. Thus, we reject days with a possible passage of cold fronts (associated with a relatively quick decrease in equivalent potential temperature).

3. Filter 3: From days passing filters 1 and 2, only those with (daily) rainfall accumulation less than 0.5 mm are retained, to avoid possible fair-weather days but with storm formation.

Table 2 presents the number of remaining days after applying each filter at the three sites. Finally, 188, 135 and 114 days are selected at HER, CRA and SLV sites respectively as days with appropriate synoptic conditions for the development of mountain breezes. The second part of the algorithm strictly detects mountain-breeze events observed during the selected days by using wind-direction measurements from the local towers. The algorithm checks if the 10-m wind (wd at 15 m at the CRA site due to data availability) blows from the expected sector according to the expected night and daytime slope flows. In other words, we check if the wd is blowing from a sector (specified in Table 2) coming from the mountains for the nighttime events (downslope, downvalley or mountain-to-plain flows) and the inverse during the day (upslope, upvalley or plain-to-mountain flows). With this information, we detect separately both types of diurnal wind events, with their respective start and end times.

Two additional criteria are imposed. The first one determines a minimum duration for each event, fixed to three hours, to focus only on persistent events and not on short ones that can distort the statistics. The second criterion states that the wind should blow from the selected sector at least 80% of the total time of each specific event, letting the wd deviate from the selected sector for short periods of time since we have observed that the continuity of the events is sometimes interrupted by short changes in wd. It should be noted that the main intention of this work is not to perform a statistical analysis of the total number of events in a determined period, but on performing a statistical characterisation of *reliable* cases. Therefore we prefer to be strict in the filters and in the additional criteria of persistence and continuity. Additionally, a few events passing all the criteria but with some missing data have been removed from the analysis.

4. Results: Description of mountain breezes at each site

4.1. HER site

Figure 1b and c show wind roses for nighttime (b) and daytime (c) breezes respectively at the HER site. Nighttime mountain flows (downslope) blow typically from the same W-WNW direction, where the closest mountains are found (see Figure 1a). The events-mean wd is 291° with a small range of variation (standard deviation, sd of 8°), highlighting the wind-direction persistence among all the events.

The nighttime events at the HER site have the weakest mean 10-m ws compared to the other sites (1.28 m s^{-1}), as well as the smallest variability. We hypothesize that the proximity of the mountain prevents the downward acceleration of the katabatic flows at this location, inhibiting high wind speeds but producing clear and repetitive katabatic events.

The daytime events at the HER site are normally more intense than nighttime ones (1.86 m s^{-1} versus 1.28 m s^{-1}). This is due to local-scale processes dominating nighttime downslope flows compared to the upslope flows (which include plain-to-mountain flows). Daytime events have a mean wd of 139° and more variability (21°) than nighttime events (see the different wind roses in Figure 1b and c).

Two examples of nighttime and daytime breezes at the HER site are shown in Figure 1d, e, f and g. The two sharp changes in wd show the arrival and end of the events, which are marked with thick blue and red lines for nighttime and daytime events, respectively. The example in Figure 1d shows a representative case in which the downslope flow arrives at the site just after the sign change of H from positive to negative, marked with a red vertical solid line. The wd remains almost constant until H changes from negative to positive (yellow vertical solid line). Wind speeds are very light (below 1.5 m s^{-1}) during the event (Figure 1f) even falling below 1 m s^{-1} at times. Mean values for all nighttime events are shown with a blue-dotted line, highlighting the representativeness of the example shown. The variability of all the events (sd, shadows) shows a constant wd with very low ws (less than 2 m s^{-1}).

The daytime event in Figure 1e also starts just after H changes from negative to positive. The event continues until H becomes negative in the evening, with the wind progressively veering from E to S during the event. This tendency is also observed in the mean and variability of all the events (red dotted line and shadow respectively). In fact, the progressive veering towards S results from the increasing influence of the plain-to-mountain thermally-driven wind associated with the larger-scale basin, which dominates the local upslope flow (from E-SE) observed during the early daytime hours. The ws increases during the event (for the example and for all the events), with wind-speed maxima occuring during the middle of the day (≈2 m s^{-1}) and decreasing towards the afternoon transition.

4.2. CRA site

A constant dominant wd is also observed for the nighttime breezes at the CRA site (Figure 2): winds from S but with a slight E component (mean of 159° with sd of 14°). The southerly flow is associated with the expected valley-wind descending through the Aure Valley, which was also observed in modelling studies in the area (Jiménez and Cuxart, 2014).

For the daytime breezes, the wind-direction variability is also greater than for the nighttime events, in agreement with the HER site. This is because the daytime breezes interact with fewer topographical features that are able to channel the wind in a specific direction (more open areas). In addition, since the turbulence intensity is considerably greater during the daytime, the flow is less directionally coherent. The mean daytime breeze direction is N, however directions shifted slightly to the E occur more frequently (see wind rose in Figure 2c), as observed for the nighttime events.

Two representative examples of nighttime and daytime mountain breezes at the CRA site are also shown in Figure 2d, e, f and g. The nighttime-event example (Figure 2d, thicker blue line) arrives at the site almost 2 h after the change in sign of H from positive to negative, slightly veering from SE to SSE until H becomes positive in the morning. It represents quite well the mean wind-direction tendency observed for all the events (blue dotted line). The wd shows minimal variability and becomes more southerly as the night progresses. Wind-speed

maxima for nighttime events are normally observed during the central part of the night, associated with the veering to the S (Figure 2f, dotted line). The example has a wind-speed maxima (>5 m s^{-1}) at 0330 UTC that exceeds the typical wind speeds at this site.

The daytime event example in Figure 2e and g arrives at the site 1 h after H changes to positive values in the morning, lasting until 1 h before H becomes negative in the afternoon. Winds are from the NE during the first part of the day and from N from 1100 UTC onward. The maximum ws for the example is observed around 1200 UTC (Figure 2g), slightly exceeding the typical conditions (marked with red shadow). A tendency of wind maxima during the central hours of the day is also observed.

4.3. SLV site

The dominant wd during nighttime at the SLV site is SE (Figure 3), where the highest peaks of the Wasatch Range are found, despite that the mountains in this direction are farther ($\approx$ 30 km) than mountains in other directions (for example, the mountains towards the E are only 15 km from the site). We think many downslope flows are formed along the slopes on the SLV side of the Wasatch Range; therefore, what we measure at the SLV site is the integrated effect of all these descending flows together with a downvalley flow channelled by the mountain corridor in the SSE direction (see Figure 3a), as suggested by Zumpfe and Horel (2007) (see their Figure 1). Nighttime breezes at the SLV site are the more intense (mean of 2.74 m s^{-1}) and also exhibit more ws variability than the other two sites. This variability is due to the complexity of the site, with mountains in almost all the directions.

The observed mean wd for the daytime events is 291°, with a dominant wd from W (wind rose in Figure 3c). That is, wind during daytime events comes from the lake but it also blows in the expected upvalley direction. In fact, in our analysis, it is difficult to distinguish between the lake breeze front and the upvalley wind since both directions are expected to be quite similar at the site. However, a common feature is observed from the analysis of several detected cases: at the beginning of the daytime events, the wd is predominantly northwesterly, while it is only later in the afternoon that winds become westerly (the example in Figure 3e is a representative case showing this feature). We think this could indicate that upvalley thermally-driven winds are first observed at the site, followed by a combination of the upvalley wind and lake daytime breeze. In any case, the interaction between lake breezes and mountain breezes at this site has been investigated exhaustively by other authors (Zumpfe and Horel, 2007) and is out of the scope of this study. The wind intensity of these daytime breezes at the SLV site is similar than for the nighttime flows. They also have a relatively large range of variation, which is the result of the combination of lake breeze and mountain thermally-driven flows.

It is more difficult to find a prototype mountain breeze event at the SLV site due to the higher variability between the events. Figure 3d shows a nighttime event formed 2 h after H becomes negative with the wind blowing from SE, with highly variable ws (Figure 3f) and a maximum ws of over 5m s^{-1} at the end of the event. The event ends 2.5 h after H changes to positive when the wind veers towards the daytime-events directions. The wd mean and sd for all the events are similar to those of the example, but the ws shows more variability.

The daytime event shown in Figure 3e and g is formed 1 h after H changes from negative to positive values, slightly veering during the day from N to W and ending around 2 h after H becomes negative. This tendency to veer from N to W is also observed in the mean and sd (dotted line and red shadow in Figure 3e). As observed for the other sites, the ws maxima are normally found during midday or even slightly later, with ws decreasing towards the transitions (Figure 3g). The example has a ws maximum of more than 5 m s^{-1}, which exceeds the typical values found for all the analysed events.

5. Results: Comparison of mountain-breezes features between sites

This section includes the site-comparison of different mountain-breezes features: arrival times, duration and synoptic conditions associated with the events.

5.1. Arrival times

Figure 4 shows the time of arrival for nighttime (left) and daytime (right) events, expressed in relation to the hour when H changes sign from positive to negative (left) or from negative to positive (right). This facilitates a comparison between the sites since the sign change in H is a good indicator of the local evening and morning transitions. Note that this arrival time can differ from the formation time at the location where the breeze is formed.

The nighttime breeze arrival at the HER site is normally observed very close to the time when H changes sign to negative values (most of the events are observed between -0.5 and +0.5 h, Figure 4a). In fact, almost 80 nighttime events arrived at the site approximately 30-minutes after the sign change in H (Figure 4a). This shows that the change from non-nighttime wd to directions within the appropriate sector is observed just after the sign change in H (recall 30-min averaged data are used). The example shown in Figure 1d illustrates this behaviour well. However, the arrival times also display variability, with some events formed between -5 and +5 h with respect to the sign change of H. The nighttime events formed before H changes sign at the HER site are sometimes observed when the synoptic wd coincides with the katabatic one (result not shown).

The distributions for CRA and SLV (Figure 4c and e) are slightly different. They are shifted to positive values, that is, the arrival of nighttime events is normally observed approximately between +0 and +4 h after H changes sign. This is also a consequence of the distance of the mountain influencing the site; i.e., katabatic flows at the HER site are observed as soon as the surface cools due to the proximity of the influencing slope, while there is a delay in the observation of the breezes at the CRA and SLV sites.

A similar behaviour is observed for daytime breezes (Figure 4b, d and f). The arrival times at the HER site occur close to the H sign change (to positive) and slightly later at the CRA site. As shown in Figure 4f, larger variability is observed at the SLV site mainly due to the influences of the lake. In any case, fewer events have been analysed for the SLV site. The fact that some daytime events at the SLV site are observed before H becomes positive is possibly due to earlier intrusions of winds from the same wd sector as the expected daytime breeze. In fact, these cases are differentiated at the SLV site, with NW winds coming from nearby Antelope Island (where there is a mountain with an elevation of almost 2000 m asl

(Figure 3a)). In these few cases, the algorithm confuses the arrival of the upvalley breeze with a downslope flow coming from this isolated mountain. This is an unavoidable short-lived issue (only in a few 30-min averages of the data, normally not more than 1 h) that is due to site complexity.

5.2. Duration

In typical and clear diurnal cycles, the duration of nighttime and daytime mountain breezes is determined by the sunlight duration. Figure 5a and b show the mean duration of the events for the three sites. The observed variability is mainly related to the variation of the sunlight duration throughout the year. Thus, longer nighttime events are observed during the winter months and vice versa for daytime breeze events (Figure 5c and d). This feature is especially evident at the CRA site. At the SLV site, where only the period from 27 December to mid-July has been analysed, the variability is also caused by the interaction between mountain and lake-generated flows that can significantly alter the initiation and end of the events. Note that Figure 5c and d indicates the number of mountain breezes detected and analysed at each site, which is smaller for the SLV site.

The lower percentiles of the boxplots presented in Figure 5a and b (i.e., short events) are due to sudden changes in the atmospheric conditions or also because some events are formed later than expected for similar reasons (with the associated diminished duration). It is worth noting that the nighttime events are longer than the daytime ones (comparison of Figure 5a and b). In fact, some nighttime events persist for more than 24 h (outliers at the CRA and SLV sites are shown in Figure 5a). All the outliers at the CRA site are observed in winter (also seen in Figure 5c). In these cases, the downslope flows persist during the daytime due to the weak daytime-heating of the surface in elevated areas because of the snowpack. One persistent-case is observed at the SLV site, also during winter (27 December case, 48 h of duration), but this is never observed at the HER site.

In contrast, daytime breezes never persist more than one day. However, some daytime breezes at the SLV site can persist into the first part of the night (not shown), shifting the distribution to larger-duration values (Figure 5b). We think that this is caused by the close proximity of the lake to the site and the higher specific heat of the water, delaying the day-night wd change associated with the lake breezes, as observed in other studies close to the sea (Soler et al., 2014; Hu and Xue, 2016). The daytime breezes that form earlier at the SLV site can also have a longer duration.

5.3. Synoptic conditions

Supplemental material shows a comparison between 10-m wind (upper figures) and 700 hPa wind from NCEP (bottom figures) at the HER (Figure S1), CRA (Figure S2) and SLV (Figure S3) sites. This information is divided into: the entire analysed period (left), periods with nighttime-breeze events (middle); and periods with daytime-breeze events (right).

At the HER site (Figure S1), the comparison between Figure S1a and Figure S1b highlights the common character of nighttime breezes in the area (the signal of nighttime events is clear in the entire-data windrose), which represents 26% of the total period (1 year). Note that we have chosen to ignore non-clear events, so this percentage could be even higher.

However, the daytime events only represent 14% of the period analysed, and their signal (Figure S1c) is weaker in Figure S1a. In addition, daytime events are also distributed over a wider sector of wind directions.

The 700-hPa windrose (Figure S1d) shows how westerlies dominate at the HER site, with wind speeds considerably larger (9.26 m s^{-1}) than those found for mountain breezes events both in the nighttime (Figure S1e) and daytime (Figure S1f) windroses (Table 3). The daytime events are associated with weaker 700-hPa winds (mean of 4.8 m s^{-1}, Table 3) than nighttime breezes, which have a mean 700-hPa ws of 6 m s^{-1} (Table 3). On the other hand, a preferred 700-hPa wd is not observed when the mountain breezes are present.

At the CRA site (Figure S2), nighttime events occur during 17% of the analysed period, and their signal (Figure S2b) is clear in the windrose (Figure S2a). However, daytime events only occur 5% of the time and their signal (Figure S2c) is weak in Figure S1a. Moreover, an additional common westerly and stronger 10-m wind is observed in the windrose (Figure S2a), which is associated with other synoptic conditions typical of the area. Analysis of the 700-hPa windroses at the CRA site (Figure S2d, e and f) leads to a conclusion similar to one found for the HER site (see Table 3); i.e., the daytime events are usually associated with weaker ws (mean of 4.9 m s^{-1}, Table 3) than the nighttime events (mean of 6 m s^{-1}, Table 3).

At the SLV site, both nighttime (Figure S3b) and daytime (figure S3c) wind signals are clear for the 10-m winds (Figure S3a), representing 13% and 8% of the total analysed period, respectively. These 10-m wind directions (especially the nighttime-breezes shown in Figure S3b) are largely decoupled from the synoptic wind (figure S3e and figure S3f), which highlights the independence of the surface-wind systems from upper-level flows. The mean 700-hPa ws during nighttime events is also higher (mean of 6.1 m s^{-1}, Table 3) than the corresponding daytime events (mean of 5.6 m s^{-1}, Table 3). The mean 700-hPa wind speeds at the SLV site are slightly lower (7 m s^{-1}, Table 3) than those at the HER and CRA sites. This is likely a result of the fact that fewer months have been analysed, including some persistent high-pressure situations.

6. Results: Mountain breezes and CO_2

6.1. CO_2 mixing ratios during mountain breezes

Figure 6 shows CO_2 mixing ratio anomalies observed for the examples (events) presented in Figure 1, Figure 2 and Figure 3 at the HER, CRA and SLV sites respectively. The upper figures show the temporal evolution for the nighttime events (blue lines) and the lower figures for daytime events (red lines). To make the results comparable between the sites, we work with CO_2 anomalies rather than absolute values. The CO_2 anomaly has been calculated by subtracting the daily mean CO_2 mixing ratio from each 30-minute average CO_2 mixing ratio data. The all-events mean CO_2 mixing ratio is indicated with green dotted lines and the standard deviation with a green shaded region.

At the HER site, the nighttime CO_2 evolution example (Figure 6a) shows a sharp increase of more than 10 ppm. This increase occurs approximately when the nighttime breeze arrives at the site during the evening transition (note how later we analyse the link between both processes). It is followed by relatively large CO_2 fluctuations throughout the night. The

anomalies are always positive until a sharp decrease occurs during the morning transition when the event ends. The example represents appropriately the mean and sd values for all the events. Thus, typically, an almost constant mean positive anomaly of around +4-5 ppm is observed during the nighttime breezes.

At the CRA site (Figure 6b), the expected and typical CO_2 mixing ratio increases and decreases around the afternoon and morning transition respectively are more gradual in the example. They are observed approximately when the nighttime breeze arrives or ends (Figure 2d and f). The increase in CO_2 anomaly starts around sunset and remains positive during the night. A maximum value coincides with the maximum ws, which is followed by a CO_2 mixing ratio decrease at the end of the event (coinciding with H changing from negative to positive). The observed tendency for all the events shows increasing CO_2 mixing ratio during the night and maximum values during the second part of the night.

At the SLV site (Figure 6c), the CO_2 mixing ratio during the nighttime-event example shows an important increase of more than 30 ppm coinciding with the establishment of the nighttime mountain-breeze event around 0300 UTC (2000 LST, Figure 3d and f). As observed at the other sites, the CO_2 mixing ratio is highly variable during the night until the decrease observed towards the morning transition, which also coincides (in this event) with the end of the nighttime mountain breeze. The mean CO_2 mixing ratio anomaly at the SLV site show, by far, the highest variability and the most extreme values in comparison with the other sites (note the larger range of the y-axis limits in Figure 6c).

We now consider daytime events. At the HER-site (Figure 6d), the example shows how the morning CO_2 decrease happens 1.5 h before the daytime event (upslope) arrives at the site, while the afternoon increase is observed just after its end. The CO_2 mixing ratio anomaly during the day remains quite constant and always well below the daily mean (-5 ppm). Mean values shows a similar tendency and a range of variability which is almost always in negative values.

At the CRA site (Figure 6e), the CO_2 mixing ratio decreases in the example well before the onset of the daytime plain-to-mountain wind (Figure 2e), but it coincides with the gradual turning of the wind from S to NE observed from 0630 UTC to 0830 UTC, with the expected start of photosynthesis and with the progressive growing of the mixing layer. During the day, the CO_2 remains quite constant. However, a decrease of a few ppm is observed from 1300 UTC to 1700 UTC, which seems to be a general tendency when analysing all the events. The CO_2 mixing ratio in the example increases in the afternoon when H becomes negative. This is associated with the establishment of a stable boundary layer, which favours the accumulation of CO_2 close to the surface. However, this increase in CO_2 mixing ratio also coincides with the gradual turning of the winds from N to S (Figure 2e).

At the SLV site (Figure 6f), the CO_2 anomaly during the daytime-event example is characterised by a sharp decrease in the mixing ratio coincident with the establishment of the breeze. The values remain almost 30 ppm lower than the daily average during the central part of the daytime, coinciding with the maximum observed ws (Figure 3g).

Although the examples of events here shown are representative of the mountain breezes observed at the sites, the case-by-case analysis of events also shows variability (as indicated by the green shaded regions in Figure 6). This motivates the climatological analysis of all the

events. Figure 7a and b show data-distribution plots for the mean CO_2 mixing ratio anomaly (with respect to the daily mean) for all nighttime (a) and daytime (b) breeze events analysed at the three sites. As expected, the anomaly is mostly positive for nighttime events, while it is negative for daytime events. On the one hand, at night, photosynthesis ceases, while plant respiration continues leading to an increase in the net CO_2 mixing ratio observed close to the surface. Simultaneously, the lower part of the planetary boundary layer becomes stable and typically experiences reduced turbulence. These two effects lead to increased near-surface CO_2 concentrations. During daytime, plants remove CO_2 through photosynthesis and the formation of a convective boundary layer helps to mix CO_2 molecules into much larger volumes of air, diminishing the net CO_2 mixing ratio observed close to the surface. Additionally, other processes contribute to the measured CO_2 close to the surface, such as soil moisture and temperature evolution, mixing from upper layers, horizontal transport (advection), respiration of heterotrophic organisms (microbes and animals) within the soil and anthropogenic activities acting as sources close to the measurements sites.

A great part of the variability observed in Figure 7a and b for each site is because of the seasonal character of the CO_2 diurnal oscillations. This is observed in Figure 7c and d at the HER site (in blue) and at the CRA site (in green), with the highest mean CO_2 mixing ratio anomalies during late spring/early summer. During these months, the diurnal cycle of CO_2 is amplified due to the enhanced difference between daytime photosynthesis and nighttime respiration of the vegetation, especially under fair weather days, which are precisely the conditions needed for the development of mountain breezes.

Maximum CO_2 uptake during daytime and emission during nighttime occurred at the HER site during late spring (April-May), corresponding to the growing season when plants (deciduous tree and annual herbs) are functional. In summer (June-September), water deficits caused leaf senescence in herbs and stomata closure in trees, decreasing CO_2 uptake by vegetation and ecosystem respiration. In autumn after soil re-wetting, the Mediterranean grasslands slightly recover but the deciduous trees lose their leaves decreasing CO_2 uptake. Moreover, in autumn low temperatures decrease the CO_2 emitted by soil respiration.

At the CRA site, there is a delay in the maximum CO_2 emissions at night and maximum CO_2 uptake during the day, having the maxima values in June/July. This delay with respect to the HER site is due to the colder character of this site and because June/July are quite wet months in this area.

This seasonal analysis cannot be done at the SLV site due to the lack of data from July onward. However, an interesting marked CO_2 peak in February due to the prevalence of high-pressure systems over the area is observed. These conditions led to a very stable environment and to the formation of persistent cold-air pools, causing high CO_2 mixing ratios during nocturnal thermal inversions and amplified diurnal cycles due to the mountain/lake breezes circulations (Whiteman et al., 2014).

On the other hand, recall that the heights of the open-path sensors were different at the HER (8 m), CRA (30 m) and SLV (10 m) sites. A priori, the highest mixing ratios would be expected at the HER site (at least during nighttime when the vertical mixing is limited), since the sensor is much closer to the surface and more influenced by 'surface activity'. However, the mixing ratios at the HER and CRA sites are similar. This is because the ws

is considerably stronger for the nighttime mountain breezes at the CRA site (mean of 2.46 m s^{-1}) in comparison with the HER site (1.28 m s^{-1}).

Figure 7d shows the differences between daytime breezes throughout the year at the three sites. The seasonal tendency for nighttime breezes is toward more negative CO_2 anomalies during spring and less negative during summer and autumn. The lowest observed peaks at the SLV site in Feb/Mar are also due to the enhanced CO_2 mixing ratio diurnal cycle.

6.2. Mountain breezes effects on CO_2

The mountain-breezes examples presented in Figure 6 show that increases (decreases) in CO_2 mixing ratio are observed around the morning (afternoon) transitions. This time coincides approximately with the arrival and end of the mountain breezes. Thus, one would be tempted to assume that these sudden changes in CO_2 mixing ratio are due to the advection caused by the wd changes associated with the breezes arrival. That is, one might hypothesise that drastic changes in CO_2 are caused by the drastic changes in wd, which may bring air from regions with different CO_2 mixing ratios from different nearby sites (i.e., sources/sinks). But, the transition from a convective to a stable boundary layer (and vice versa) is also observed around these times. These periods are also associated with the ending (starting) of photosynthesis, with drastic changes in the strength of the surface turbulence and with the change in the sign of H, which alters the energy available to mix the lowest layers of the planetary boundary layer.

Hence, the main question is: what role do mountain breezes play in the observed CO_2 increases and decreases as well as in the evolution of the CO_2 mixing ratio throughout the events. To address this question, we have adopted the following strategy: 1) analyse the timing of the maximum CO_2 increase with respect to the arrival of nighttime mountain breezes; 2) relate the CO_2 mixing ratio relationship with the observed surface turbulence during nighttime, and; 3) examine the CO_2 mixing ratio values for different ranges of wind directions under similar conditions of turbulence.

6.2.1. Time of maximum CO_2 increase (initiation) with respect to the arrival time of nighttime breezes to the site

Typically, an increase in the CO_2 mixing ratio is observed during the evening transition. We have computed the time when this CO_2 increase starts as the time in which the CO_2 mixing ratio data show a larger difference with its value 1 h later. Thus, this value indicates the time when the CO_2 mixing ratio starts to increase (always with respect to the maximum CO_2 increment observed). This time is, in some cases, coincident with the arrival of the nighttime breeze, but not always. To analyse this, we have computed this offset time as the difference between the time of initiation of the maximum CO_2 increase and the time of arrival of the nighttime-breeze event (Figure 8)

For the example shown in Figure 6a and Figure 1d at the HER site, the CO_2 increase starts at the same time that the nighttime-breeze event arrives at the site; hence, this event has an offset time of 0 h in Figure 8. Since we are using 30-min averaged data, an offset time of -0.5 h also indicates a very good correlation between the time of CO_2 increase and

the initiation of the breeze event since it coincides with the latest time block with a wd out of the range of nighttime events.

As observed in Figure 8, a large percentage of the offset times are between -0.5 and 0 h at the HER (38%), CRA (22%), and SLV (24%) sites, which indicates that both phenomena (arrival of descending flow and initiation of the maximum increase in CO_2 mixing ratio) are observed at the same time. However, this is not always the case, and the time of initiation of the maximum CO_2 increase is variable in the rest of the cases. In fact, it is also common to observe some events in which the CO_2 increase occurs several hours after the arrival of the nighttime breeze (positive values in Figure 8), and there are a few cases where the CO_2 increase is observed several hours before the breeze arrival.

It is also worth noting that the sum of the percentages for each site do not equal 100 % because some events do not show a significant CO_2 maximum increase at these times (a minimum value of 5 ppm/h has been imposed for the increase). Moreover, in some cases, the CO_2 increase is not clear during the 3 h preceding or following the arrival of the nighttime-breeze event. In addition, we have selected the maximum observed 1-h CO_2 increase because the observed CO_2 increase is normally a quite rapid phenomenon; however, in some cases (especially at the SLV site), the CO_2 increase is more gradual and takes longer to achieve the maximum CO_2 mixing ratio. As a result, there are cases without a clear 1-h CO_2 increase around the analysed period. In any case, after inspecting the behaviour of the CO_2 at the three sites, the HER site shows the clearest CO_2 diurnal cycle, while the CO_2 behaviour in many events observed at the other two sites is more complex and (in some cases) not clearly linked to the mountain breezes nor even to the afternoon/evening transition.

These results suggest that the CO_2 increase and the arrival of nighttime breezes are often observed at similar but not always simultaneous times. The variability in these offset times indicates that the advection of CO_2 produced by a drastic change in wd (i.e., mountain breezes) is not the main cause of the (normally) observed increase in CO_2 mixing ratios during the afternoon/evening transition. Thus, the change from a convective to a stable boundary layer, the decrease in turbulence in the afternoon transition and the cease of photosynthesis are processes that should have more importance in the measured CO_2 concentration than the pure advection produced by the breezes.

6.2.2. CO_2 mixing ratio and surface turbulence relationship

Figure 9 shows the mean CO_2 mixing-ratio anomaly with respect to the daily mean during the nighttime events as a function of the TKE. Since some nighttime-breeze events are also observed during part of the daytime, we have limited the analysis to nighttime to avoid large daytime TKE values (normally associated with positive CO_2 anomalies). The results are shown with different line colors for each site. The plots show how maxima CO_2 mixing-ratio anomalies are associated with specific ranges of TKE.

At the HER site (blue line), the maximum CO_2 values are observed when the TKE is between 0.1 and 0.15 m^2s^{-2}. When the TKE values are lower, the observed CO_2 mixing ratio are also lower, which is due to weak turbulence mixing near the surface, inhibiting CO_2 transport to the measurement height (8 m at the HER site). However, the mean CO_2 mixing ratio also decreases for TKE values above the commented maximum-CO_2 threshold (0.15

m^2s^{-2}). This is due to the enhanced vertical mixing, and hence, dilution of CO_2 molecules.

This is also well observed at the CRA site but with a higher TKE threshold (0.3 to 0.5 m^2s^{-2}), which is due to the fact that the open-path instrument was installed at a higher elevation (30 m agl). Hence, higher levels of turbulence are needed to reach the maximum CO_2 mixing ratios. We have analysed this characteristic at the CRA site using CO_2 sensors installed at different heights during a different period (BLLAST field campaign (Lothon et al., 2014)). This analysis (not shown here) illustrates how, indeed, the maximum CO_2 mixing ratio is associated with lower TKE levels for observations taken closer to the surface.

At the SLV site, where the sensor was installed at 10 m, the maximum CO_2 mixing ratio occurs at low TKE levels (0.025 to 0.05 m^2s^{-2}). These values are considerably lower than those found at the HER site, where the sensor was located at a similar height (8 m). However, above 0.1 m^2s^{-2} the SLV-site curve looks very similar to the HER-site curve. The maximum CO_2 levels at the SLV site occurs at much lower TKE values because the nighttime events analysed at the SLV site in February are associated with very stable conditions (valley cold-air pools), producing extremely low levels of turbulence which result in high values of CO_2. These results at the SLV site are supported by other research conducted during this period in nearby areas (Lin et al., 2018).

Mountain breezes are expected to interact with the local turbulence by changing the near-surface wind profile. Therefore, the CO_2-TKE relationship here found represents an indirect (but important) effect of mountain breezes on CO_2. This effect complicates the interpretation of the CO_2 measurements (not only concentrations, but also vertical and horizontal fluxes) during the night under these conditions, as discussed in the literature (Feigenwinter et al., 2008).

6.2.3. CO_2 mixing ratio and wd relationship

Finally, we attempt to determine the effect of wd on CO_2 mixing ratios at each tower site. Figure 10 shows the mean CO_2 mixing ratio anomaly observed during nighttime mountain-breeze events for different wd ranges. To standardize the vertical mixing conditions, the data have been limited to periods with controlled values of TKE, corresponding to the maximum CO_2 anomalies shown in Figure 9. The following values of TKE have been used to filter the data: 0.025-0.2 m^2s^{-2} (80% of data) at the HER site; 0.05-0.3 m^2s^{-2} (61% of data) at the CRA site, and; 0-0.1 m^2s^{-2} (77% of data) at the SLV site. By doing this, we avoid comparing CO_2 mixing ratios with very different turbulence conditions, which can lead to undesired differences for specific ranges of wd.

At the HER site (Figure 10a), slightly lower CO_2 mixing-ratio anomalies are found for directions between 285° and 320°. Some residential areas are found in this sector from the tower site, with less vegetation than directions more towards the W and less influenced by (weak) anthropogenic sources more to the N. In any case, the area surrounding this site is quite homogeneous in terms of land use. The small towns surrounding the site have limited CO_2 emissions leading to very small differences (only 1 ppm in Figure 10a), which are statistically insignificant.

At the CRA site (Figure 10b), larger differences in CO_2 mixing ratios between different wind directions exist (maximum difference of ≈4-5 ppm). The wind directions associated

with the maximum CO_2 mixing ratio come from an industrial area in the nearby town of Lannemezan, which could act as a significant CO_2 source.

The largest mixing ratio variability as a function of wd is found at the SLV site (Figure 10c), where Salt Lake City and the Wasatch Front metropolitan area have an important influence on CO_2 concentrations. Maximum mixing ratios are found when the wd is 125°, which coincides with directions associated with the city airport and SLC city centre. Lower CO_2 mixing ratios are found for more southerly winds (even negative CO_2 mixing ratio anomalies), where residential areas are found with less industrial activities and more vegetation. In any case, it should be noted that only limited data exist for these wd ranges during nighttime events at the site (26 and 15 as stated above the bars Figure 10, corresponding to 13 and 7.5 h of data of wind coming from these sectors).

The results discussed in the previous paragraph show how the wd has a relatively small impact on the observed CO_2 mixing ratio at sites without significant heterogeneity in terms of land use/land cover (i.e., at the HER site). However, the impact slightly increases at the CRA and SLV sites, where the land use is more heterogeneous. At the SLV site, the existence of a large city leads to numerous important emission sources associated with specific wd (as supported by other studies (Huang et al., 2015; Lin et al., 2018)). Therefore, the relative importance of nighttime advection on CO_2 is highly site-dependent, especially in complex terrain regions influenced by mountain breezes. This result is in accordance with the findings of previous studies (e.g Aubinet and Feigenwinter, 2010; Aubinet et al., 2010).

7. Conclusions

A systematic mountain-breeze detection algorithm has been used to detect nighttime (downslope, downvalley or mountain-to-plain) and daytime (upslope, upvalley or plain-to-mountain) flow events. The analysis has been performed at three different sites: (i) close to the Guadarrama Mountains (HER), (ii) a plateau close to the Pyrenees (CRA), and (iii) a location within the Salt Lake Valley (SLV).

In terms of wd, nighttime events have a smaller range of wd compared to daytime breezes. This difference is imposed by the topography (i.e., the wind of daytime breezes blow from relatively flat areas less affected by important topographical features capable of imposing directionality in the winds).

Regarding the ws, the larger the scale of the thermally-driven flow, the more intense the wind. This result is in accordance with previous findings which state that downslope flows speed up with downslope distance (see Zardi and Whiteman (2013) and references herein). Hence, the nighttime breezes at the HER site (the site with the closest mountain) are weaker than at the other two sites.

The comparison between nighttime and daytime ws is also modulated by the particularities of each sites. At the HER site, the daytime breezes have a larger scale than nighttime ones, and, therefore, they are more intense. At the CRA site, daytime breezes are slightly less intense than nighttime ones, due to the possible deceleration effect of the convective boundary layer (diminishing temperature gradients). At the SLV site, the combination

of a lake breeze and upvalley flow results in daytime breezes with wind speeds similar to nighttime descending flows.

The timing of arrival of the mountain breezes to the sites is related to the time of the buoyancy heat flux sign change. Both phenomena are often coincident at the HER site, while a delay of a few hours is usually observed at the CRA and SLV sites (there are larger distances from the mountains to the site).

The seasonal variation of the breezes is determined by the sunlight duration, but the nighttime breezes at the three sites have longer durations than daytime ones. In addition, the comparison between the 700 hPa ws during the nighttime and daytime flows show how the daytime events are only observed when the synoptic winds are weaker. These lead us to conclude that the formation of daytime breezes is more difficult than nighttime ones.

We also analyse the effects of these breezes on CO_2 mixing ratios. As expected, the mean CO_2 mixing ratio anomaly during a breezes is positive during the nighttime and negative during daytime events. The seasonal variation is also well observed with an increased CO_2 diurnal cycle during late spring/early summer. At the SLV site, the CO_2 mixing ratios are markedly higher than at the two other sites during the nighttime events due to an amplified diurnal cycle of the CO_2 mixing ratio caused by the contrasting differences in wd during nighttime events (coming from the Salt Lake City with high CO_2 mixing ratio) compared to daytime events (air coming from the Great Salt Lake with weaker CO_2 mixing ratio). This feature is enhanced in February (2015) due to the persistence of cold-air pools in the area.

The direct link between mountain breezes and observed CO_2 mixing ratios during afternoon and morning transitions was analysed. First, although the typical CO_2 increase in the afternoon transition is often almost coincident with the arrival of the nighttime breezes, sometimes both phenomena have an offset of a few hours, which unlink a direct relation between the CO_2 increase and the advection caused by the arrival of the breeze. Second, the CO_2 mixing ratio during the nighttime events is controlled by the strength of turbulence. We have identified TKE threshold values in which the CO_2 mixing ratio at some height is maximum. TKE values above this threshold are associated with lower CO_2 mixing ratios due to enhanced mixing, which diffuses the CO_2 into larger volumes of air. TKE values below the threshold are also associated with lower CO_2 mixing ratio, due to the less-effective mixing between shallow layers rich in CO_2 and air layers at the observation height. The TKE threshold value at the CRA site is larger than at the other two sites since more energy is needed to mix the lower layers up to the observation height (30 m). Finally, the analysis of the relation between CO_2 mixing ratio and the wd during the nighttime events revealed how significant differences are only found for the SLV site, where the CO_2 emission from the city influences the measurements taken at the measurement point depending on the wd.

These results suggest that the mountain breezes impact the CO_2 concentrations in two ways. First, it is well known these phenomena change the vertical wind profiles and, therefore, the wind shear and the turbulence close to the surface, influencing the CO_2 measurements during the nighttime events. On the other hand, the advection effect of mountain breezes on CO_2 measurements seems to be important in regions with contrasting surfaces with different emission areas, where these winds can transport air with different concentration of CO_2. At sites with more homogeneous sources and sinks, the horizontal CO_2

transport by the mountain breezes is less important than other mechanisms such as biological activity, vertical turbulent mixing, and stabilisation of the lower layers of the PBL.

In any case, field experiments with an appropriate deployment of instruments (in the vertical and in the horizontal) are needed to further investigate the role of advection and how air is transported from and over the mountainous areas and to better investigate the role of the turbulent mixing at different heights. Moreover, a more exhaustive analysis of the sources and sinks of CO_2 and soil-plant activities is needed to better understand the observed evolution in CO_2.

Acknowledgements

This research has been funded by the ATMOUNT-II project [Ref. CGL2015-65627-C3-3-R (MINECO/FEDER)], the Project Ref. CGL2016-81828-REDT/AEI from the Spanish Government, and by the GuMNet (Guadarrama Monitoring Network, www.ucm.es/gumnet) observational network of the CEI Moncloa Campus of International Excellence. We thank the contribution of all the members of the GuMNet Team, especially Dr. J.F. González-Rouco, and Patrimonio Nacional for the facilities given during the installation of the meteorological tower. Jon A. Arrillaga is supported by the Predoctoral Training Program for No-Doctor Researchers of the Department of Education, Language Policy and Culture of the Basque Government (PRE_2017_2_0069, MOD = B). Observation data at the CRA site were collected at the Pyrenean Platform for Observation of the Atmosphere P2OA (http://p2oa.aero.obs-mip.fr). P2OA facilities and staff are funded and supported by the Observatoire Midi-Pyrnes (University of Toulouse, France) and CNRS (Centre National de la Recherche Scientifique). P2OA is part of ACTRIS-FR French Infrastructure. A portion of the research was also funded by the Office of Naval Research Award #N00014-11-1-0709, Mountain Terrain Atmospheric Modeling and Observations (MATERHORN) Program. Thanks to NCEP for the NCEP-FNL data: National Centers for Environmental Prediction/National Weather Service/NOAA/U.S. Department of Commerce. 2000, updated daily. NCEP FNL Operational Model Global Tropospheric Analyses, continuing from July 1999. Research Data Archive at the National Center for Atmospheric Research, Computational and Information Systems Laboratory. https://doi.org/10.5065/D6M043C6. Accessed 28-02-2018. We acknowledge Wunderground.com for the daily rainfall data at the SLV site.

References

Alekseychik, P., Mammarella, I., Launiainen, S., Rannik, Ü., Vesala, T., 2013. Evolution of the nocturnal decoupled layer in a pine forest canopy. Agric. For. Meteorol. 174, 15–27.

Araújo, A. C., Kruijt, B., Nobre, A. D., Dolman, A. J., Waterloo, M. J., Moors, E. J., Souza, J. S., 2008. Nocturnal accumulation of co2 underneath a tropical forest canopy along a topographical gradient. Ecol. Appl. 18 (6), 1406–1419.

Arrillaga, J. A., de Arellano, Vil-Guerau de Arellano, J., Bosveld, F., Baltink, H. K., Yagüe, C., Sastre, M., Román-Cascón, C., 2018. Impacts of afternoon and evening sea-breeze fronts on local turbulence, and on co2 and radon-222 transport. Quart. J. Roy. Meteor. Soc. 144 (713), 990–1011.

Arrillaga, J. A., Yagüe, C., Sastre, M., Román-Cascón, C., 2016. A characterisation of sea-breeze events in the eastern cantabrian coast (spain) from observational data and wrf simulations. Atmos. Res. 181, 265–280.

Aubinet, M., Feigenwinter, C., 2010. Direct co2 advection measurements and the night flux problem. Agric. For. Meteorol. 150 (5), 651–654.

Aubinet, M., Feigenwinter, C., Heinesch, B., Bernhofer, C., Canepa, E., Lindroth, A., Montagnani, L., Rebmann, C., Sedlak, P., Van Gorsel, E., 2010. Direct advection measurements do not help to solve the night-time co2 closure problem: Evidence from three different forests. Agric. For. Meteorol. 150 (5), 655–664.

Baldocchi, D., Falge, E., Gu, L., Olson, R., Hollinger, D., Running, S., Anthoni, P., Bernhofer, C., Davis, K., Evans, R., et al., 2001. Fluxnet: A new tool to study the temporal and spatial variability of ecosystem–scale carbon dioxide, water vapor, and energy flux densities. Bull. Amer. Meteor. Soc. 82 (11), 2415–2434.

Baldocchi, D. D., 2003. Assessing the eddy covariance technique for evaluating carbon dioxide exchange rates of ecosystems: past, present and future. Global Change Biol. 9 (4), 479–492.

Doran, J. C., Fast, J. D., Horel, J., 2002. The VTMX 2000 campaign. Bull. Am. Meteorol. Soc. 83 (APRIL), 537–551.

Durán, L., Rodríguez-Muñoz, I., Sánchez, E., 2017. The peñalara mountain meteorological network (1999–2014): Description, preliminary results and lessons learned. Atmosphere 8 (10), 203.

Eugster, W., Siegrist, F., 2000. The influence of nocturnal co2 advection on co2 flux measurements. Basic Appl. Ecol. 1 (2), 177–188.

Feigenwinter, C., Bernhofer, C., Eichelmann, U., Heinesch, B., Hertel, M., Janous, D., Kolle, O., Lagergren, F., Lindroth, A., Minerbi, S., et al., 2008. Comparison of horizontal and vertical advective co2 fluxes at three forest sites. Agric. For. Meteorol. 148 (1), 12–24.

Fernando, H., Pardyjak, E., Di Sabatino, S., Chow, F., De Wekker, S., Hoch, S., Hacker, J., Pace, J., Pratt, T., Pu, Z., et al., 2015. The materhorn: Unraveling the intricacies of mountain weather. Bull. Amer. Meteor. Soc. 96 (11), 1945–1967.

Gielen, B., Loustau, D., Ceulemans, R., Jordan, A., Papale, D., et al., 2017. Integrated carbon observation system (icos): an infrastructure to monitor the european greenhouse gas balance. In: Terrestrial ecosystem research infrastructures: challenges and opportunities/Chabbi, Abad [edit.]. pp. 505–520.

Gilmanov, T. G., Aires, L., Barcza, Z., Baron, V., Belelli, L., Beringer, J., Billesbach, D., Bonal, D., Bradford, J., Ceschia, E., et al., 2010. Productivity, respiration, and light-response parameters of world grassland and agroecosystems derived from flux-tower measurements. Rangeland Ecol Manag 63 (1), 16–39.

Gultepe, I., Fernando, H., Pardyjak, E., Hoch, S., Silver, Z., Creegan, E., Leo, L., Pu, Z., De Wekker, S., Hang, C., 2016. An overview of the materhorn fog project: observations and predictability. Pure Appl. Geophys. 173 (9), 2983–3010.

Hang, C., Nadeau, D., Gultepe, I., Hoch, S., Román-Cascón, C., Pryor, K., Fernando, H., Creegan, E., Leo, L., Silver, Z., et al., 2016. A case study of the mechanisms modulating the evolution of valley fog. Pure Appl. Geophys. 173 (9), 3011–3030.

Hu, X.-M., Xue, M., 2016. Influence of synoptic sea-breeze fronts on the urban heat island intensity in dallas–fort worth, texas. Mon. Weather Rev. 144 (4), 1487–1507.

Huang, X., Wang, T., Talbot, R., Xie, M., Mao, H., Li, S., Zhuang, B., Yang, X., Fu, C., Zhu, J., et al., 2015. Temporal characteristics of atmospheric co2 in urban nanjing, china. Atmos. Res. 153, 437–450.

Jiménez, M. A., Cuxart, J., 2014. A study of the nocturnal flows generated in the north side of the pyrénées. Atmos. Res. 145, 244–254.

Karipot, A., Leclerc, M., Zhang, G., Martin, T., Starr, G., Hollinger, D., McCaughey, J., Hendrey, G., 2006. Nocturnal co 2 exchange over a tall forest canopy associated with intermittent low-level jet activity. Theor. Appl. Climatol. 85 (3-4), 243–248.

Karipot, A., Leclerc, M. Y., Zhang, G., Lewin, K. F., Nagy, J., Hendrey, G. R., Starr, G., 2008. Influence of nocturnal low-level jet on turbulence structure and co2 flux measurements over a forest canopy. J Geophys Res Atmos. 113 (D10).

Kutsch, W. L., Kolle, O., Rebmann, C., Knohl, A., Ziegler, W., Schulze, E.-D., 2008. Advection and resulting co2 exchange uncertainty in a tall forest in central germany. Ecol. Appl. 18 (6), 1391–1405.

Kyoto Protocol, K., 1997. United nations framework convention on climate change. Kyoto Protocol, Kyoto 19.

Lehner, M., Rotach, M., 2018. Current challenges in understanding and predicting transport and exchange in the atmosphere over mountainous terrain. Atmosphere 9, 276.

Lin, J. C., Mitchell, L., Crosman, E., Mendoza, D., Buchert, M., Bares, R., Fasoli, B., Bowling, D. R., Pataki, D., Catharine, D., et al., 2018. Co2 and carbon emissions from cities: linkages to air quality, socioeconomic activity and stakeholders in the salt lake city urban area. Bull. Amer. Meteor. Soc. (2018).

Lothon, M., Lohou, F., Pino, D., Couvreux, F., Pardyjak, E., Reuder, J., Vil-Guerau de Arellano, J., Durand, P., Hartogensis, O., Legain, D., et al., 2014. The bllast field experiment: boundary-layer late afternoon and sunset turbulence. Atmos. Chem. Phys. 14 (20), 10931–10960.

Mahrt, L., 2017. Stably stratified flow in a shallow valley. Boundary-Layer Meteorol. 162 (1), 1–20.

Mahrt, L., Mills, R., 2009. Horizontal diffusion by submeso motions in the stable boundary layer. Environ. Fluid Mech 9 (4), 443–456.

Martínez, D., Jiménez, M. A., Cuxart, J., Mahrt, L., 2010. Heterogeneous Nocturnal Cooling in a Large Basin Under Very Stable Conditions. Boundary-Layer Meteorol. 137, 97–113.

Monti, P., Fernando, H. J. S., Princevac, M., Chan, W. C., Kowalewski, T. A., Pardyjak, E. R., 2002. Observations of Flow and Turbulence in the Nocturnal Boundary Layer over a Slope. J. Atmos. Sci. 59, 2513–2534.

Nadeau, D. F., Pardyjak, E. R., Higgins, C. W., Huwald, H., Parlange, M. B., 2013. Flow during the evening transition over steep Alpine slopes. Q. J. R. Meteorol. Soc. 139 (April), 607–624.

Olson, D. M., Dinerstein, E., Wikramanayake, E. D., Burgess, N. D., Powell, G. V., Underwood, E. C., D'amico, J. A., Itoua, I., Strand, H. E., Morrison, J. C., et al., 2001. Terrestrial ecoregions of the world: A new map of life on earth. a new global map of terrestrial ecoregions provides an innovative tool for conserving biodiversity. Bioscience 51 (11), 933–938.

Pino, D., Vilà-Guerau de Arellano, J., Peters, W., Schröter, J., van Heerwaarden, C., Krol, M., 2012. A conceptual framework to quantify the influence of convective boundary layer development on carbon dioxide mixing ratios. Atmos. Chem. Phys. 12 (6), 2969–2985.

Prabha, T. V., Leclerc, M. Y., Karipot, A., Hollinger, D. Y., 2007. Low-frequency effects on eddy covariance fluxes under the influence of a low-level jet. J. Appl. Meteorol. Climatol 46 (3), 338–352.

Prtenjak, M. T., Klaić, M., Jeričević, A., Cuxart, J., 2018. The interaction of the downslope winds and fog formation over the zagreb area. Atmos. Res. 214, 213–227.

Raupach, M. R., 2011. Carbon cycle: Pinning down the land carbon sink. Nature Climate Change 1 (3), 148.

Román-Cascón, C., Yagüe, C., Mahrt, L., Sastre, M., Steeneveld, G. J., Pardyjak, E., van de Boer, A., Hartogensis, O., 2015. Interactions among drainage flows, gravity waves and turbulence: a bllast case study. Atmos. Chem. Phys. 15, 9031–9047.

Rotach, M. W., Calanca, P., Graziani, G., Gurtz, J., Steyn, D. G., Vogt, R., Andretta, M., Christen, A., Cieslik, S., Connolly, R., De Wekker, S. F. J., Galmarini, S., Kadygrov, E. N., Kadygrov, V., Miller, E., Neininger, B., Rucker, M., Van Gorsel, E., Weber, H., Weiss, A., Zappa, M., 2004. Turbulence structure

and exchange processes in an Alpine Valley: The Riviera Project. Bull. Am. Meteorol. Soc. 85 (January), 1367–1385.
Rotach, M. W., Stiperski, I., Fuhrer, O., Goger, B., Gohm, A., Obleitner, F., Rau, G., Sfyri, E., Vergeiner, J., 2017. Investigating exchange processes over complex topography: the innsbruck box (i-box). Bull. Amer. Meteor. Soc. 98 (4), 787–805.
Rotach, M. W., Wohlfahrt, G., Hansel, A., Reif, M., Wagner, J., Gohm, A., 2014. The world is not flat: Implications for the global carbon balance. Bull. Amer. Meteor. Soc. 95 (7), 1021–1028.
Serafin, S., Adler, B., Cuxart, J., De Wekker, S. F., Gohm, A., Grisogono, B., Kalthoff, N., Kirshbaum, D. J., Rotach, M. W., Schmidli, J., et al., 2018. Exchange processes in the atmospheric boundary layer over mountainous terrain. Atmosphere 9 (3), 102.
Soler, M., Udina, M., Ferreres, E., 2014. Observational and numerical simulation study of a sequence of eight atmospheric density currents in northern spain. Boundary-Layer Meteorol. 153 (2), 195–216.
Staebler, R. M., Fitzjarrald, D. R., 2004. Observing subcanopy co2 advection. Agric. For. Meteorol. 122 (3-4), 139–156.
Stewart, J. Q., Whiteman, C. D., Steenburgh, W. J., Bian, X., 2002. A climatological study of thermally driven wind systems of the us intermountain west. Bull. Amer. Meteor. Soc. 83 (5), 699–708.
Stiperski, I., Rotach, M. W., 2016. On the measurement of turbulence over complex mountainous terrain. Boundary-Layer Meteorol. 159 (1), 97–121.
Sun, H., Clark, T. L., Stull, R. B., Black, T. A., 2006. Two-dimensional simulation of airflow and carbon dioxide transport over a forested mountain: Part i: Interactions between thermally-forced circulations. Agric. For. Meteorol. 140 (1-4), 338–351.
Sun, J., Burns, S. P., Delany, A. C., Oncley, S. P., Turnipseed, A. A., Stephens, B. B., Lenschow, D. H., LeMone, M. A., Monson, R. K., Anderson, D. E., 2007. Co2 transport over complex terrain. Agric. For. Meteorol. 145 (1-2), 1–21.
Sun, J., Desjardins, R., Mahrt, L., MacPherson, I., 1998. Transport of carbon dioxide, water vapor, and ozone by turbulence and local circulations. J Geophys Res Atmos. 103 (D20), 25873–25885.
Sun, J., Mahrt, L., Nappo, C., Lenschow, D. H., 2015. Wind and temperature oscillations generated by wave–turbulence interactions in the stably stratified boundary layer. J. Atmos. Sci. 72 (4), 1484–1503.
Uebel, M., Bott, A., 2018. Influence of complex terrain and anthropogenic emissions on atmospheric co2 patterns–a high-resolution numerical analysis. Quart. J. Roy. Meteor. Soc. 144 (710), 34–47.
Uebel, M., Herbst, M., Bott, A., 2017. Mesoscale simulations of atmospheric co2 variations using a high-resolution model system with process-based co2 fluxes. Quart. J. Roy. Meteor. Soc. 143 (705), 1860–1876.
Urry, J., 2015. Climate change and society. In: Why the social sciences matter. Springer, pp. 45–59.
Whiteman, C., 2000. Mountain Meteorology: Fundamentals and Applications. Oxford University Press. 355 pp., New Jork.
Whiteman, C. D., Hoch, S. W., Horel, J. D., Charland, A., Sep. 2014. Relationship between particulate air pollution and meteorological variables in Utah's Salt Lake Valley. Atmos. Environ. 94 (c), 742–753.
Whiteman, C. D., Zhong, S., 2008. Downslope flows on a low-angle slope and their interactions with valley inversions. part i: Observations. J. Appl. Meteorol. Climatol 47 (7), 2023–2038.
Yakir, D., 2017. Biogeochemistry: Large rise in carbon uptake by land plants. Nature 544 (7648), 39.
Zardi, D., Whiteman, C. D., 2013. Diurnal mountain wind systems. In: Mountain Weather Research and Forecasting. Springer, pp. 35–119.
Zumpfe, D. E., Horel, J. D., 2007. Lake-breeze fronts in the salt lake valley. J. Appl. Meteorol. Climatol 46 (2), 196–211.

Table 1: Information about the instrumentation used in this study for each site. CS indicates Campbell Scientific, Inc. and VI indicates Vector Instruments. EC150, IRGASON and LI-COR 7500 A are open path infrared gas analyzers. CSAT3 is a three dimensional sonic anemometer/thermometer. The sonic Thies is an ultra-sonic anemometer 2D. CS A100LK and Déolia are cup anemometers and VI W200P at HER and CRA are wind vanes. All the data have been averaged to 30-min blocks. The rainfall used are daily quantities measured by rain gauges at HER and CRA site. For the SLV site, the daily rainfall has been obtained from www.wunderground.com.

	HER	**CRA**	**SLV**
CO_2, H and TKE sensor	CS IRGASON	LI-COR 7500 A	CS EC150
Height	8 m	30 m	10 m
Sampling rate	10 Hz	10 Hz	20 Hz
Wind speed sensor	CS A100LK	Déolia/Sonic Thies	CS CSAT3
Height	10 m	10 m	10 m
Wind direction sensor	VI W200P	VI W200P	CS CSAT3
Height	10 m	15 m	10 m
Rainfall	OTT Pluvio	EML ARG100	*Wunderground*

Table 2: Information about the analysed period in each site, days passing each filter, final detected nighttime and daytime events and wd sectors for each one.

Site	**Analysed period**	**Total analysed days**	**Days passing Filter 1-2-3**	**Detected nighttime events**	**Detected daytime events**	**Wind sector nighttime**	**Wind sector daytime**
HER	01-01-2017 to 31-12-2017	365	201-193-188	177	136	250°-360°	70°-230°
CRA	01-01-2017 to 31-12-2017	365	179-168-135	112	56	110°-220°	300°-50°
SLV	27-12-2014 to 15-07-2015	201	165-134-114	30	31	60°-200°	225°-360°

Table 3: 700 hPa wind speed (m s^{-1}) comparison between all analysed data and only moments with nighttime or daytime mountain-breeze events for each site. Note how at the SLV site, a shorter period has been analysed and the all-data wind could be not representative of normal yearly values at the area.

	HER	CRA	SLV
Mean ws 700 hPa - all data	9,26	9,8	7
Mean ws 700 hPa - nighttime events	6	6	6,1
Mean ws 700 hPa - daytime events	4,8	4,9	5,6

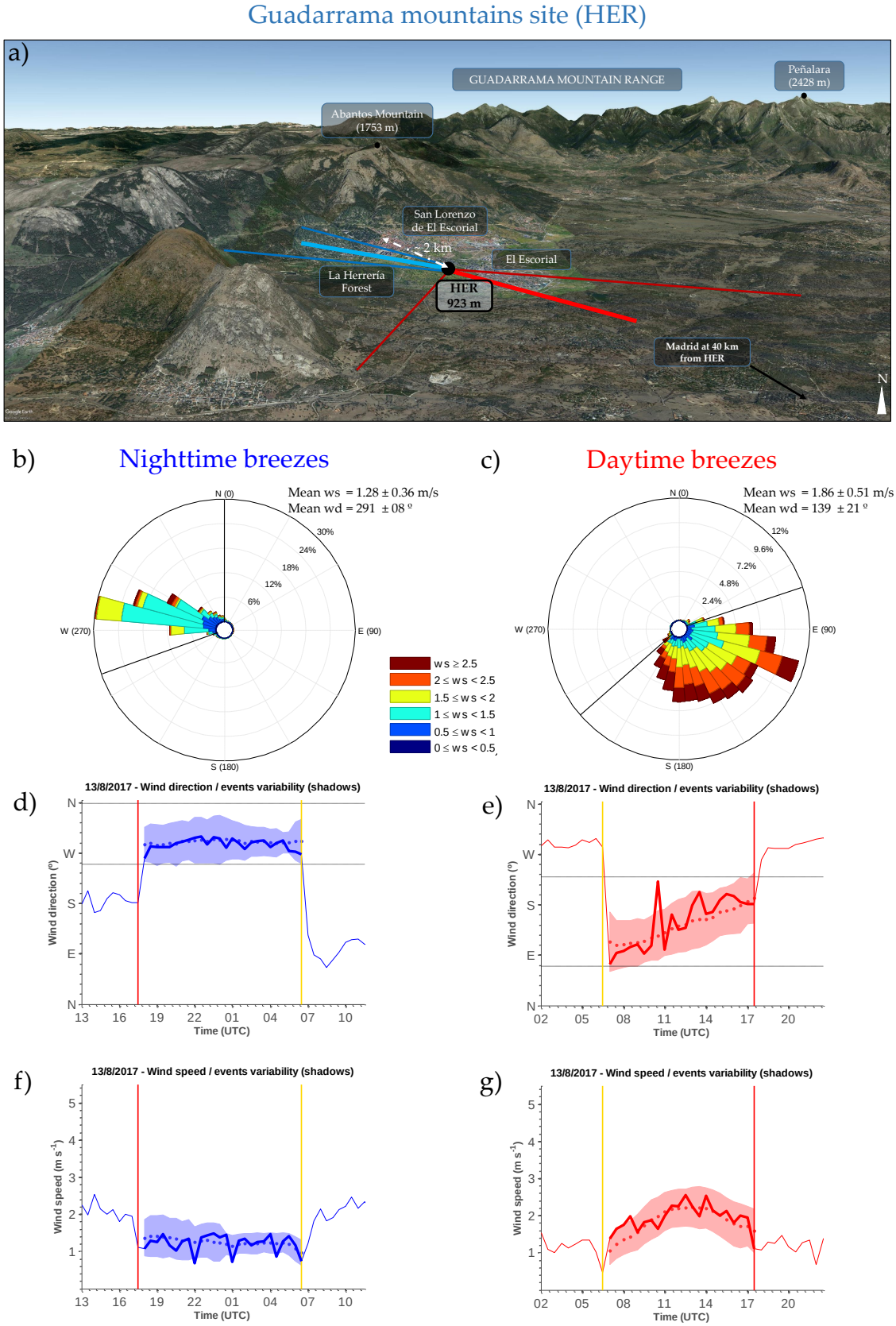

Figure 1: a) 3D Google Earth image of the HER area. The thicker blue (red) line shows mean nighttime (daytime) event wd; thinner lines indicate the approximate range of variability. North (N) is indicated in the lower right corner, but can lead to undesired optic effects due to the 3D character of the image. b) Nighttime-event wind rose using 30-min averaged data. Wind-direction range used in the algorithm is indicated between black lines. Mean and standard deviation (sd) values calculated for all the events are indicated. c) Same as *b* but for daytime breezes. d) wd for an example nighttime-breeze at the HER site (13/08/2017, LT = UTC+2) indicated with blue line (thicker one for the event duration). Vertical red (yellow) solid lines indicates the sensible heat flux change from positive to negative (negative to positive). Wind-direction mean for all events is shown with blue points and their sd with shadow (strictly for the timing of the example). Horizontal-dashed lines indicate the wind-direction range in the algorithm. e) Same as *d* but for daytime-breeze events with red colours (example for 13/08/2017, LT = UTC+2). f, g) Same as *d* and *e* but for wind speed (m s^{-1}).

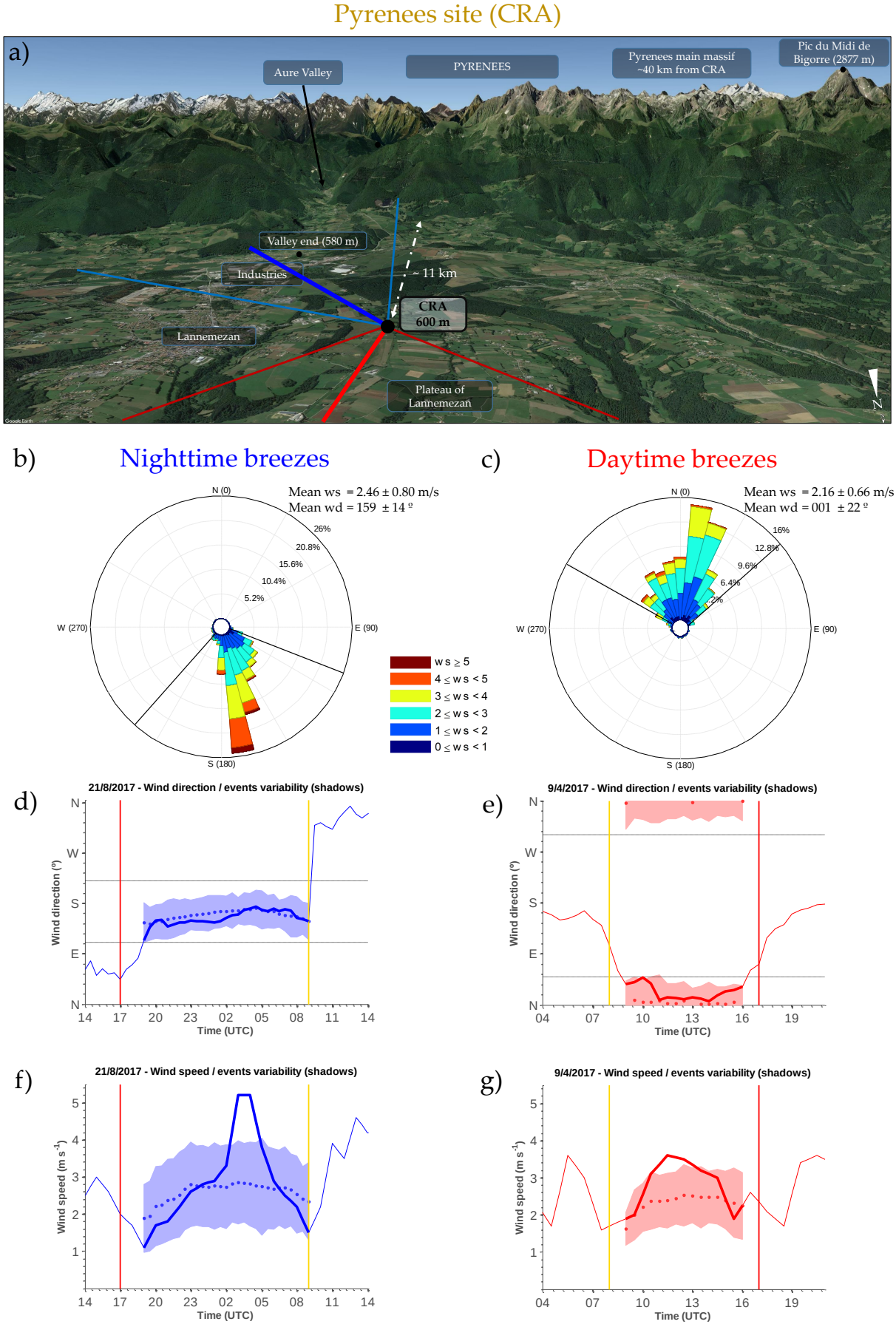

Figure 2: a) Same as in Figure 1 but for CRA. d, f) Event for 21/08/2017, LT = UTC+2. e, g) Event for 09/04/2017, LT = UTC+2.

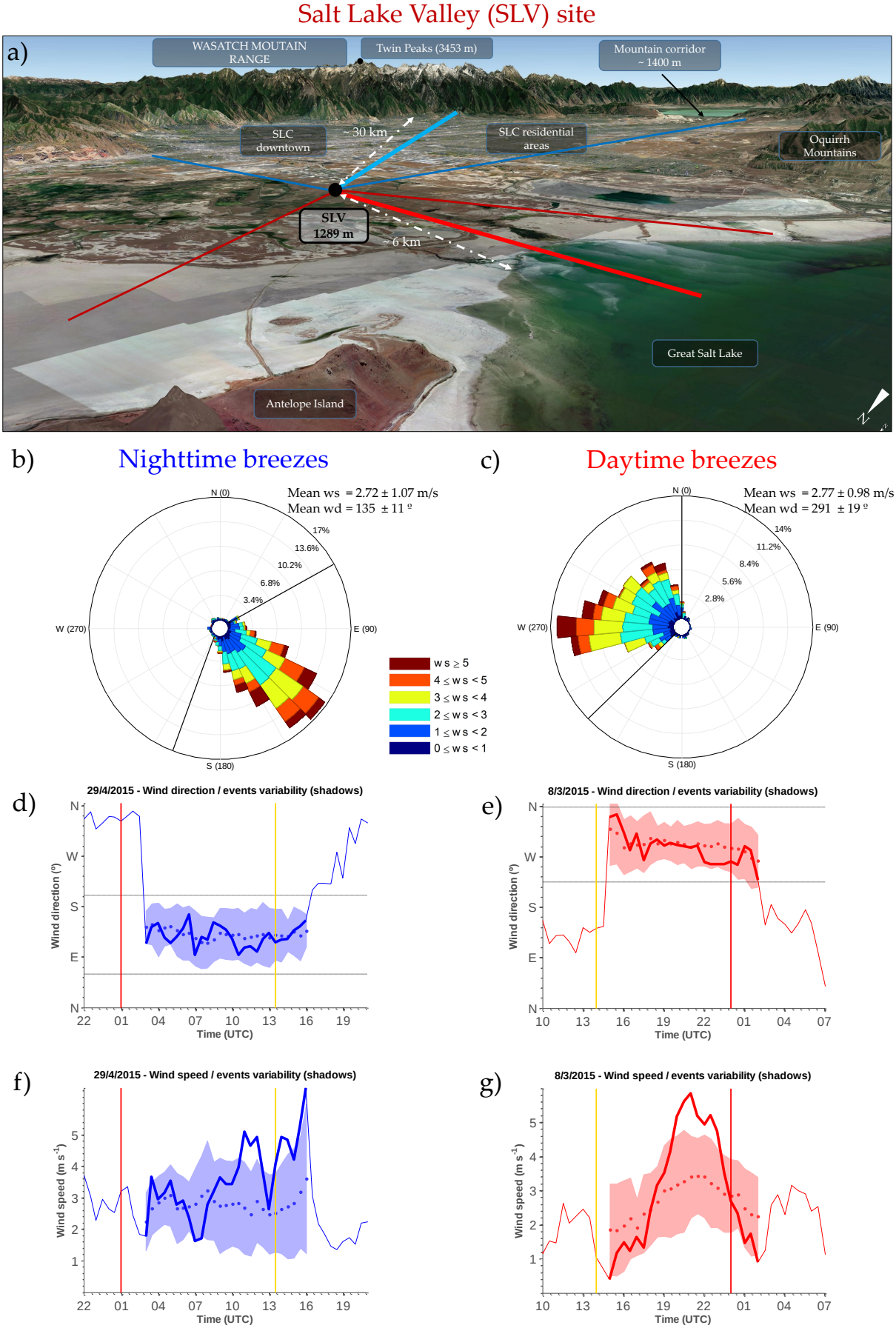

Figure 3: a) Same as in Figure 1 but for SLV. d, f) Event for 29/04/2015, LT = UTC-6. e, g) Event for 08/03/2015, LT = UTC-7.

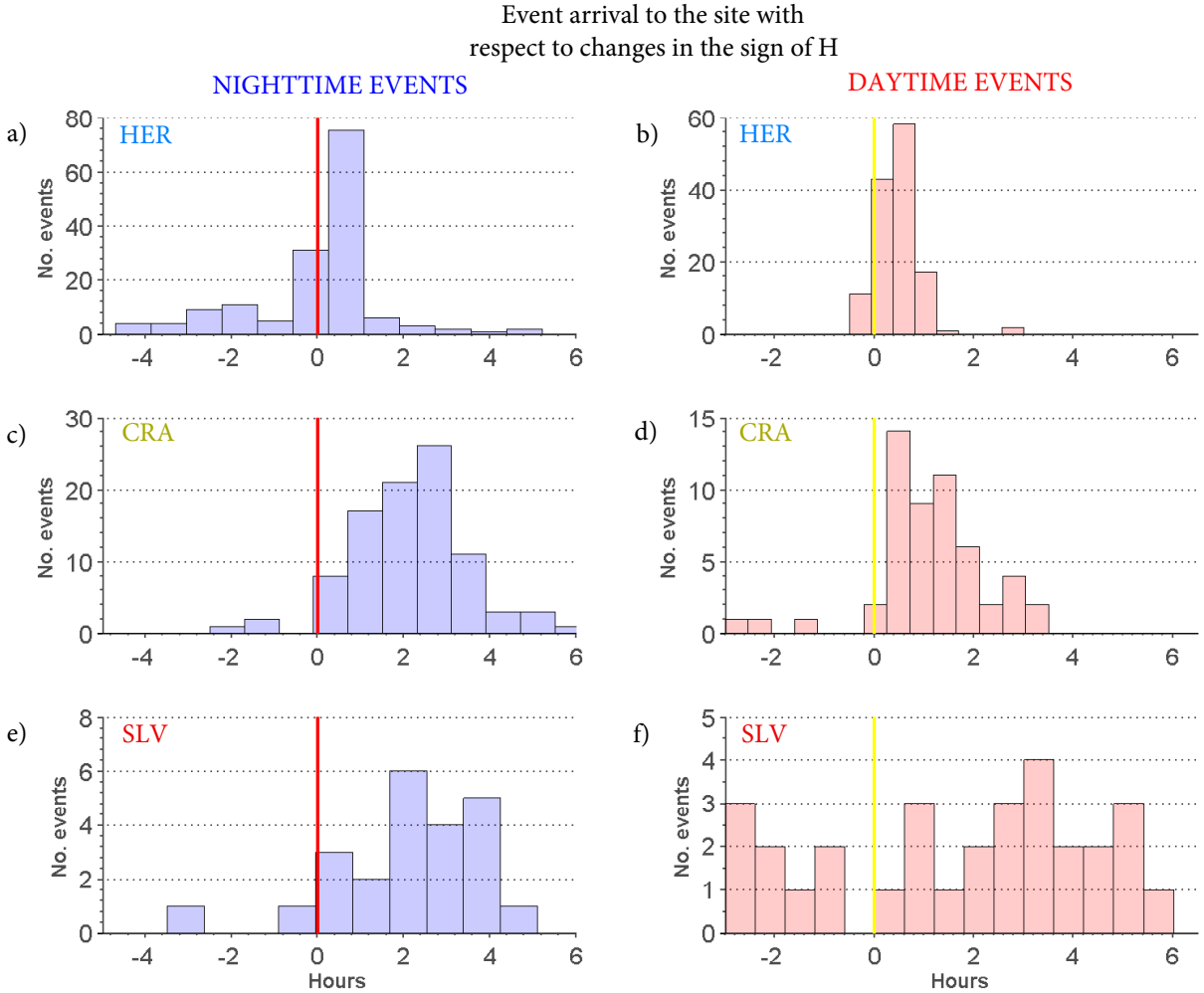

Figure 4: Number of nighttime (left, in blue) and daytime (right, in red) events (y-axis) regarding their arrival time with respect to the hour when H becomes negative (left, indicated with vertical red line) or positive (right, indicated with vertical yellow line) for HER (up), CRA (middle) and SLV (below). Example: a bar up to 75 (y-axis) around +0.5 h (x-axis) in figure a means that the arrival to the HER site of 75 events from the total detected nighttime events is observed 0.5 h after H changes from positive to negative values.

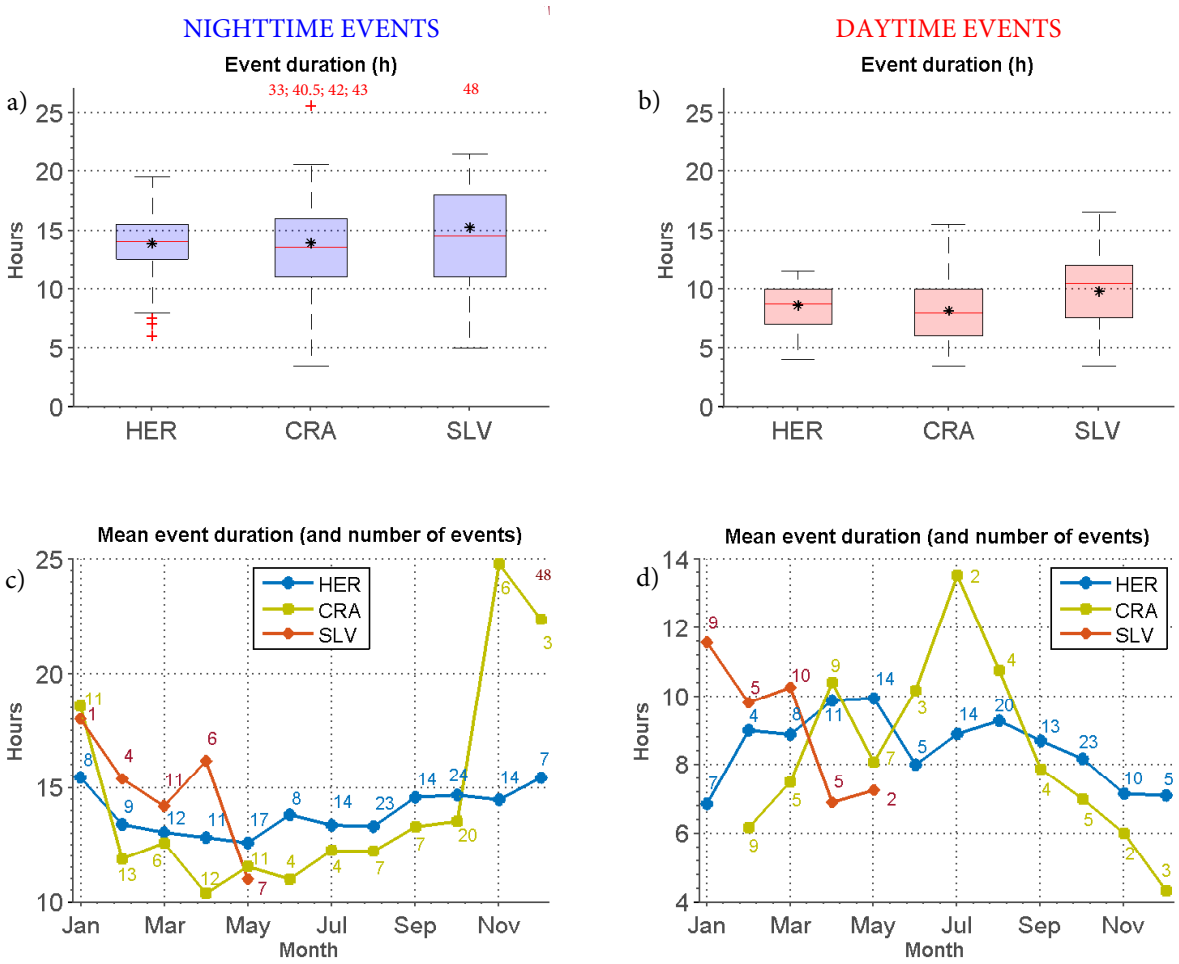

Figure 5: a, b) Event-duration distribution (in h) for nighttime (a, in blue) and daytime (b, in red) breezes detected at each site. Central boxes indicate the central 50% of the distribution, while the upper and lower remaining 25% (not considered as outliers) are indicated with the whiskers. The median of the distributions is indicated with red horizontal lines and the mean with black stars. Outliers are marked with red crosses and with numbers in red, indicating the value of duration (in h). c, d) Monthly evolution of nighttime (c) and daytime (d) events mean duration (h) for HER (blue), CRA (green) and SLV (red). Small numbers indicate the number of mountain breeze events detected and used in each month at each site.

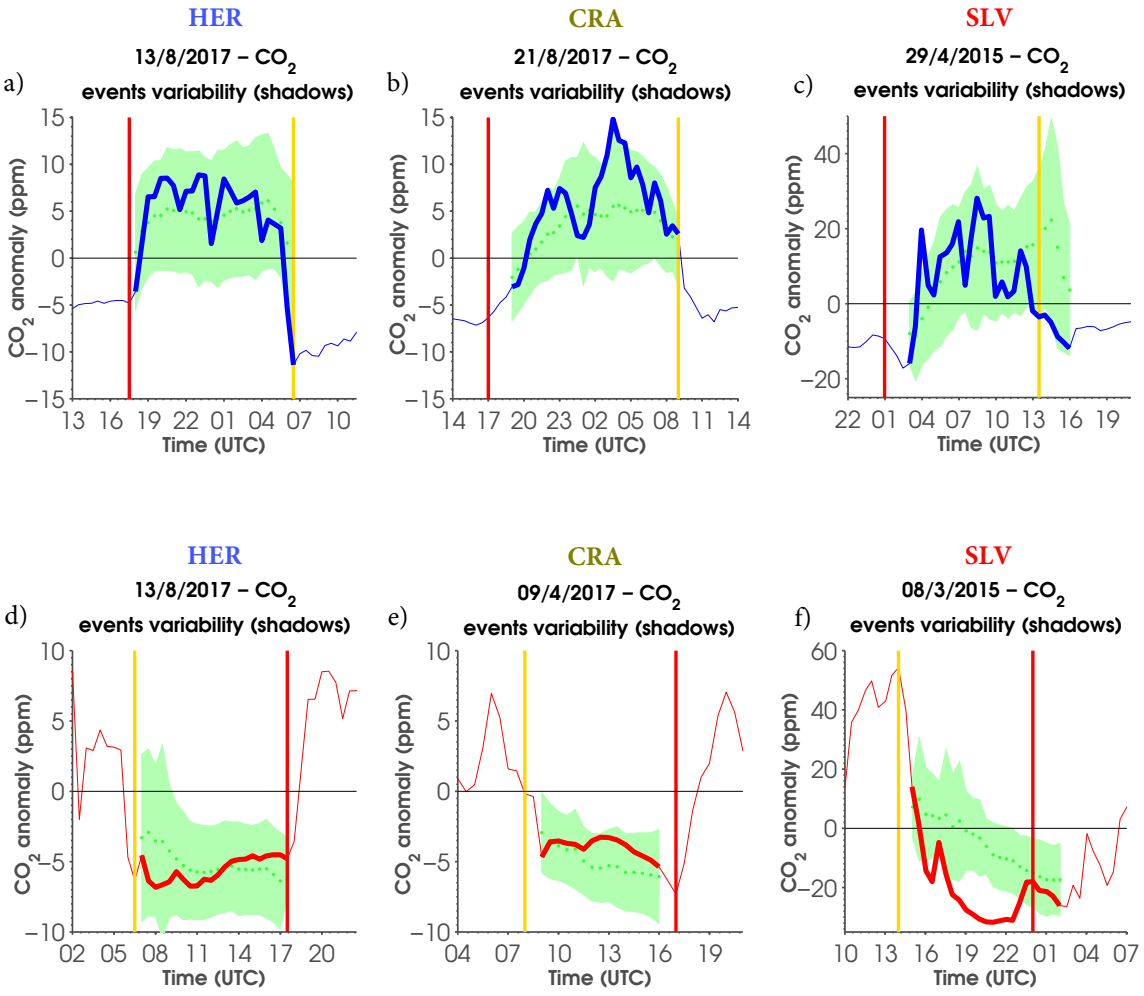

Figure 6: CO_2 mixing ratio daily anomaly evolution (in ppm) for the nighttime events examples in Figure 1, Figure 2 and Figure 3 (figures above). Vertical yellow and red lines indicate the time when H changes sign. Same as for daytime events (figures below). The blue (red) thick lines show the CO_2 mixing ratio during each event. Dotted-green lines show the mean CO_2 mixing ratio for all the events at each site. The variability (sd) is shown with green shadows. Note how the scale of SVL figures (c, f) is larger than for the other sites.

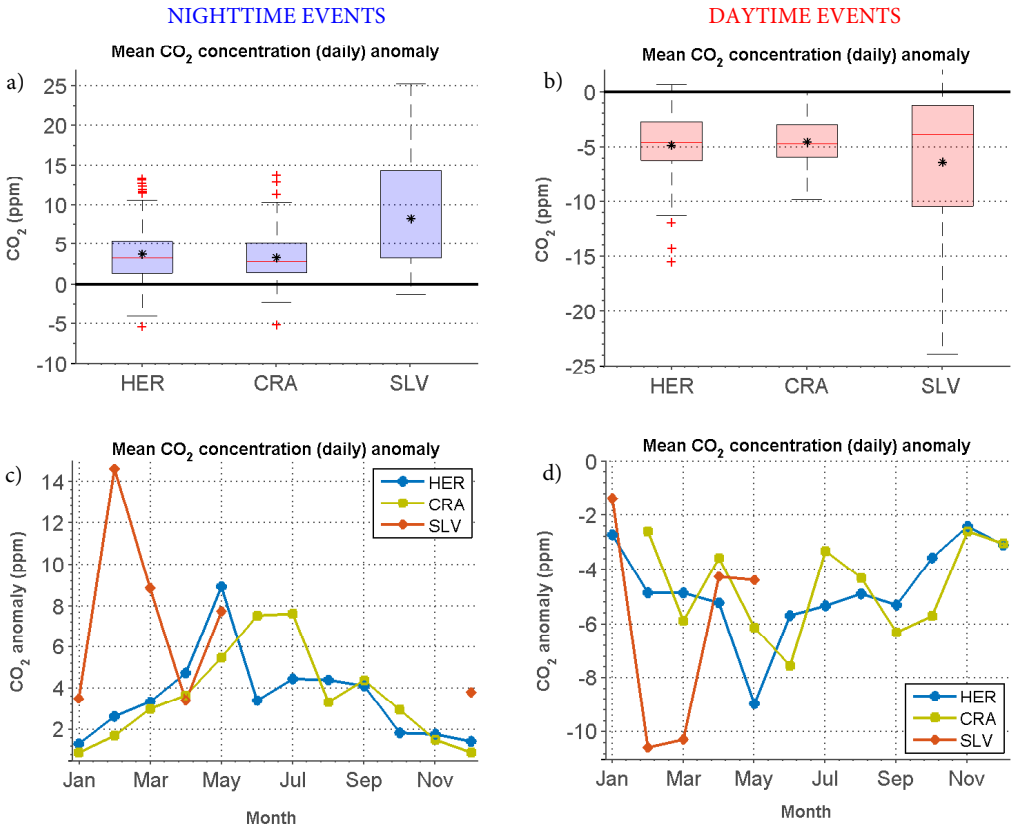

Figure 7: Data distribution plot for nighttime (left, in blue) and daytime (right, in red) breezes detected at each site for mean CO_2 mixing ratio anomaly with respect to the daily CO_2 mixing ratio mean (in ppm); c, d) Mean CO_2 mixing ratio anomaly (in ppm) with respect to the daily mean for each month at the HER (blue), CRA (green) and SLV (red) sites during nighttime (c) and daytime (d) breeze events. These mean values have been calculated using all 30-min slots data from the detected events.

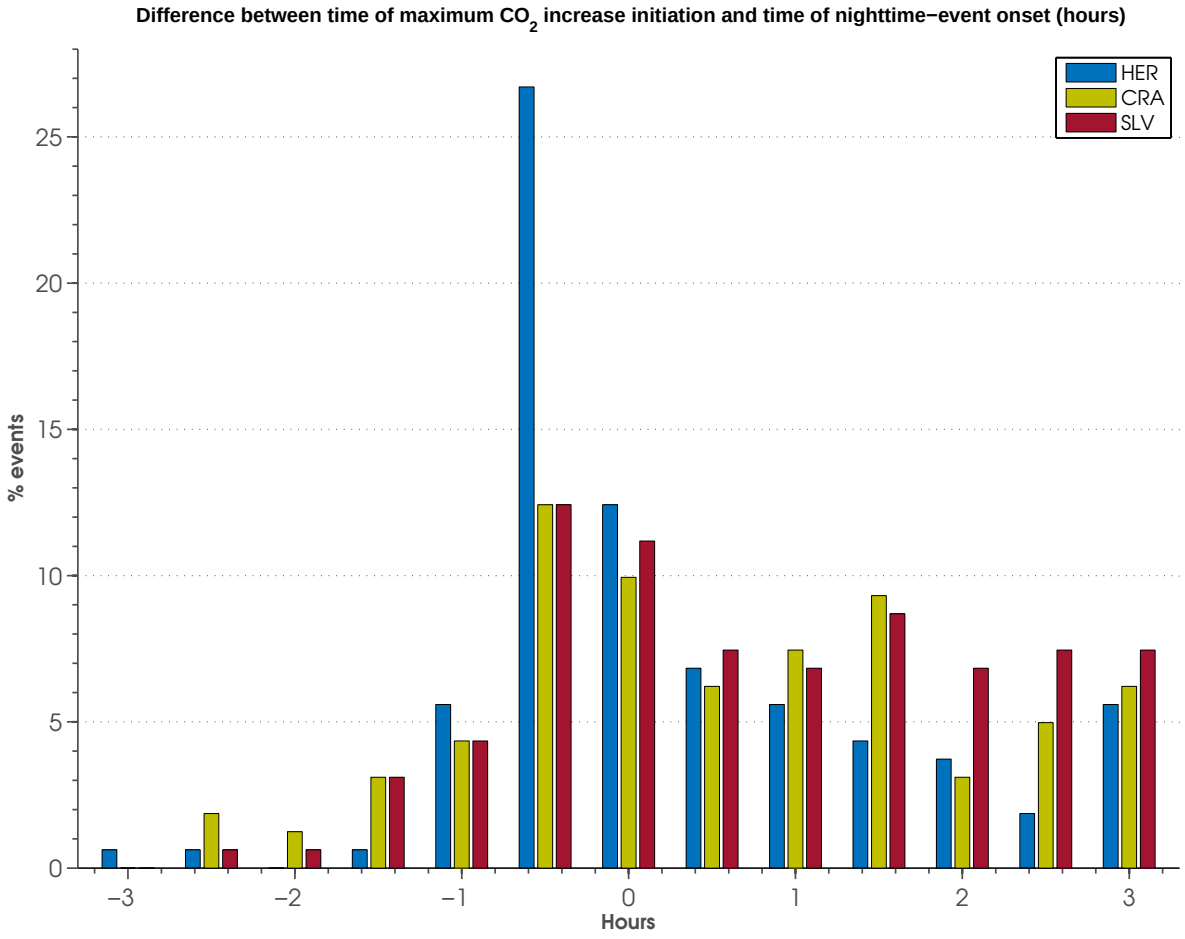

Figure 8: Percentage of events from total ones (y-axis) with time difference (in h) between the initiation time of the maximum CO_2 increase (in 1 h) and the arrival time of the nighttime event (x-axis). Example: the 27% of blue bar at -0.5 h means that the initiation of the maximum CO_2 increase (in 1 h) is observed 0.5 h before the nighttime event arrival to the site in 27% of the total detected events at the HER site. Note how only maximum CO_2 increase larger than 5 ppm have been included.

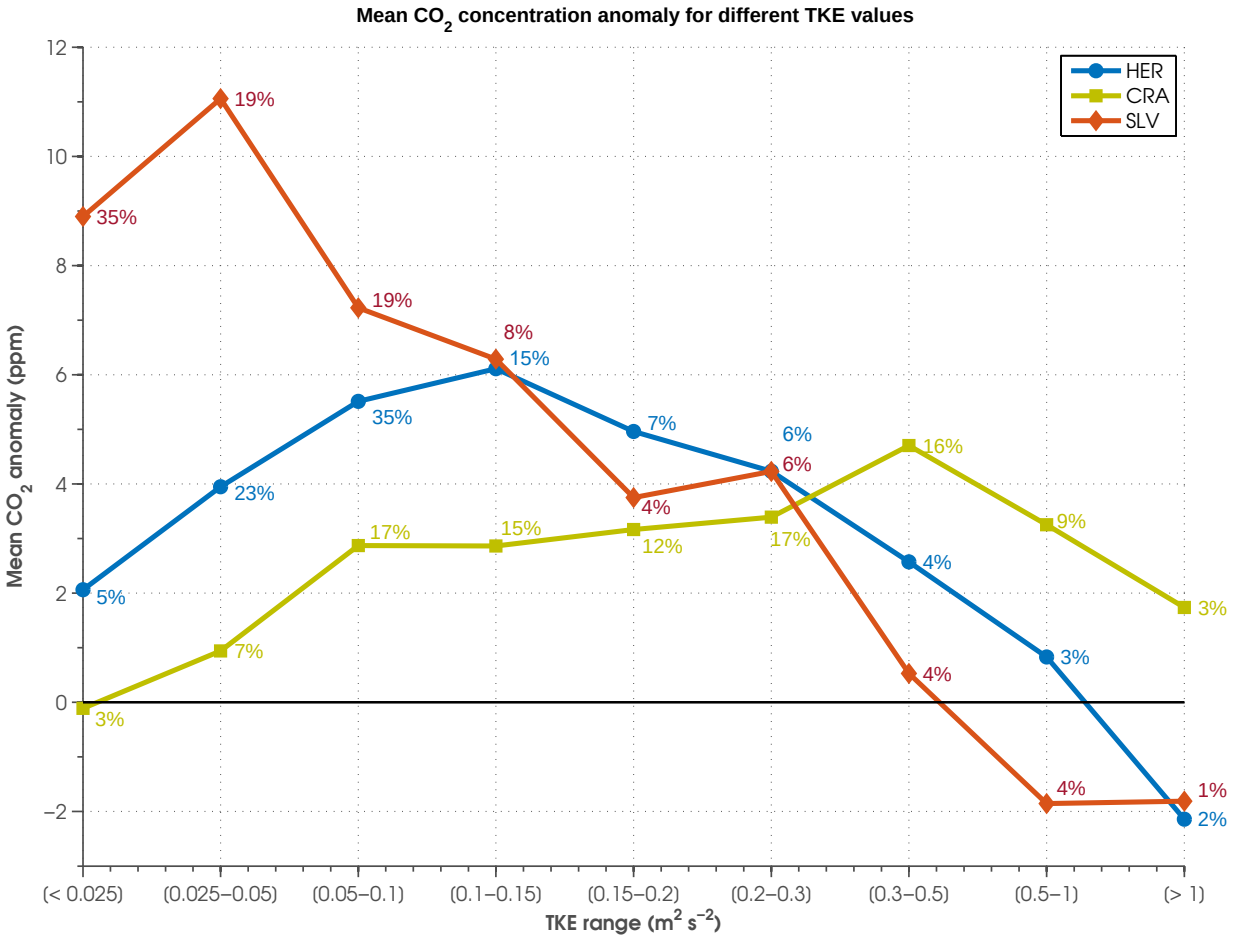

Figure 9: Mean CO_2 mixing ratio (anomaly with respect to the daily mean) in ppm associated with different ranges of values of turbulent kinetic energy (TKE) (m^2 s^{-2}) during all nighttime events at the HER (blue), CRA (green) and SLV (red) sites. Only periods strictly during nighttime have been used. Percentages in numbers represent the percentage of time with those values of TKE for all nighttime events used; for example, the first number for the SLV line (35% in red) means that TKE has values lower than 0.025 m^2 s^{-2} during 35% of nighttime-events time.

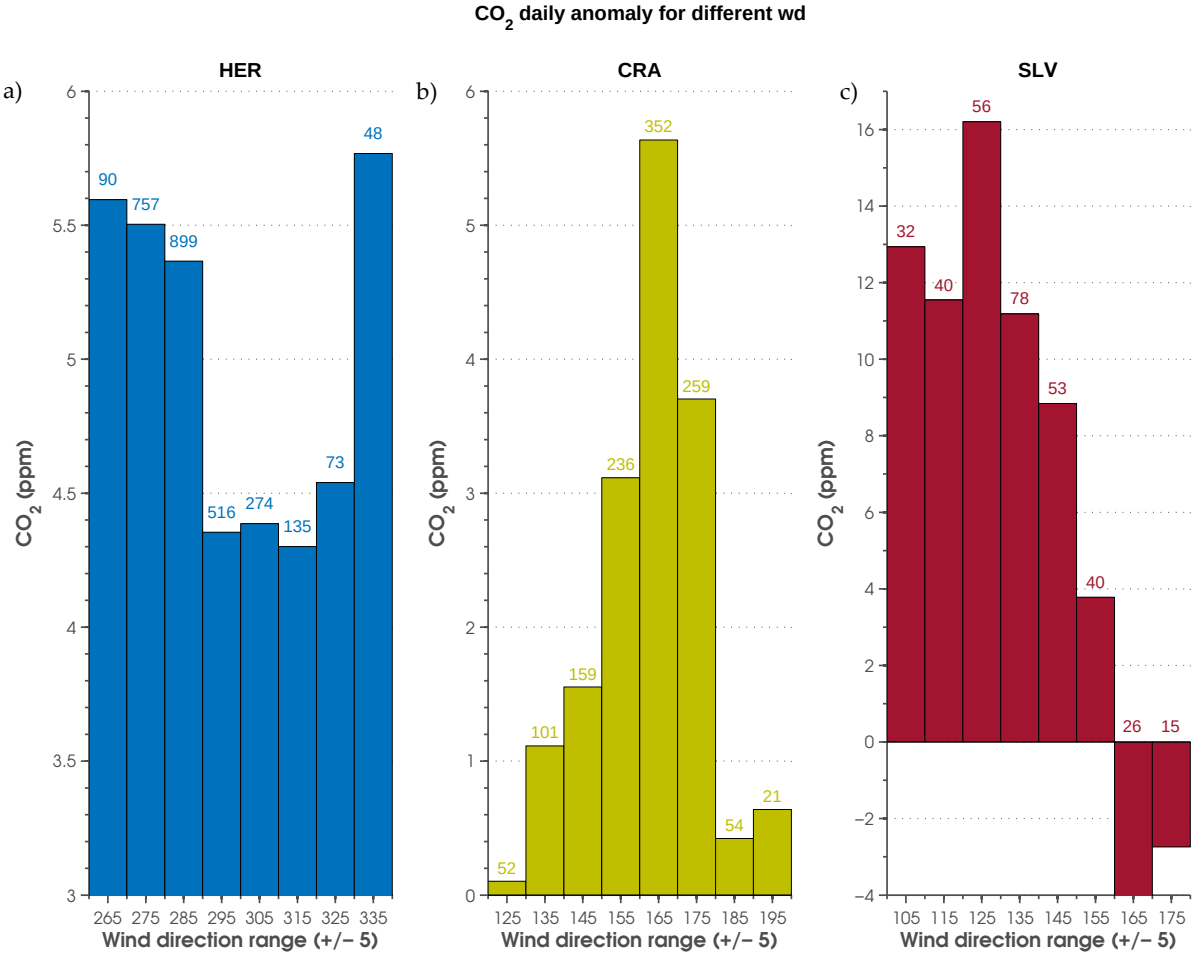

Figure 10: Mean CO_2 anomaly with respect to the daily mean in ppm (y-axis) observed for different ranges (of 10°) of wd (x-axis) for the HER (a), CRA (b) and SLV (c) sites. These ranges are around the main nighttime wd and are calculated strictly during nighttime moments (removing data during daytime) and for specific values of TKE: CRA from 0.025 to 0.2 m^2 s^{-2}; CRA from 0.05 to 0.3 m^2 s^{-2} and SLC from 0 to 0.1 m^2 s^{-2}, which correspond to the highest percentages observed in Figure 9. Numbers above the bars indicate the number of 30-min data used for the computation of the mean.